University of Alberta

Blasius Boundary Layer Flow over a Cylinder and Sphere Attached to a Wall: Characterization of Lift and Drag Forces

by

Lyle Gordon Sweeney

A thesis submitted to the Faculty of Graduate Studies and Research
in partial fulfillment of the requirements for the degree of

Master of Science

Department of Mechanical Engineering

Edmonton, Alberta
Fall 2006

Library and Archives Canada

Published Heritage Branch

395 Wellington Street
Ottawa ON K1A 0N4
Canada

Bibliothèque et Archives Canada

Direction du Patrimoine de l'édition

395, rue Wellington
Ottawa ON K1A 0N4
Canada

Your file Votre référence
ISBN: 978-0-494-22382-6
Our file Notre référence
ISBN: 978-0-494-22382-6

NOTICE:
The author has granted a non-exclusive license allowing Library and Archives Canada to reproduce, publish, archive, preserve, conserve, communicate to the public by telecommunication or on the Internet, loan, distribute and sell theses worldwide, for commercial or non-commercial purposes, in microform, paper, electronic and/or any other formats.

The author retains copyright ownership and moral rights in this thesis. Neither the thesis nor substantial extracts from it may be printed or otherwise reproduced without the author's permission.

AVIS:
L'auteur a accordé une licence non exclusive permettant à la Bibliothèque et Archives Canada de reproduire, publier, archiver, sauvegarder, conserver, transmettre au public par télécommunication ou par l'Internet, prêter, distribuer et vendre des thèses partout dans le monde, à des fins commerciales ou autres, sur support microforme, papier, électronique et/ou autres formats.

L'auteur conserve la propriété du droit d'auteur et des droits moraux qui protège cette thèse. Ni la thèse ni des extraits substantiels de celle-ci ne doivent être imprimés ou autrement reproduits sans son autorisation.

In compliance with the Canadian Privacy Act some supporting forms may have been removed from this thesis.

While these forms may be included in the document page count, their removal does not represent any loss of content from the thesis.

Conformément à la loi canadienne sur la protection de la vie privée, quelques formulaires secondaires ont été enlevés de cette thèse.

Bien que ces formulaires aient inclus dans la pagination, il n'y aura aucun contenu manquant.

Canada

Abstract

Hydrodynamic forces on a sphere attached to a plane wall and an infinite circular cylinder oriented normal to the streamwise direction and also attached to a plane wall are examined using computational fluid dynamics. The flow over the plane wall is considered to be a fully-developed Blasius boundary layer, and the flow about the geometries is limited to the steady case. Coefficient of lift and drag results are generated for sphere Reynolds numbers in the range 0.01 – 250 and in the cylinder Reynolds number range 0.06 – 49, valid at a Reynolds number with respect to plate length of 32 400. Empirical fits to the data using exponential functions are presented, which are valid in the sphere Reynolds number range 0 – 250, and in the cylinder Reynolds number range 0.06 – 49. Comprehensive grid and boundary placement convergence studies were used to confirm the simulation accuracy. In addition, the results of the sphere were validated against existing low Reynolds number analytical results and high Reynolds number experimental data. Experimental and analytical results do not exist for the cylindrical geometry.

Acknowledgements

I appreciate the support and direction of Dr. Warren Finlay over the course of this work. Additionally, I cherished the company and creative atmosphere fostered in the laboratory.

Lastly, I would like to recognise the support of the Alberta Ingenuity Fund and the Natural Sciences and Engineering Research Council of Canada.

To my family, a great source of inspiration,
and sense of wellbeing.

Contents

1 Introduction **1**
- 1.1 Background 3
- 1.2 History 6
- 1.3 Computation 9
- 1.4 Summary of Thesis 10

2 Methods and Theory **12**
- 2.1 Introduction 12
- 2.2 Mathematical Models 12
- 2.3 Numerical Method and Grid Generation 13
  - 2.3.1 Discretization 13
  - 2.3.2 Algebraic Solution of Discretized Equations 16
  - 2.3.3 Mesh Generation 17
  - 2.3.4 Force Calculation 18
- 2.4 Boundary Conditions 18
- 2.5 Dimensionless Analysis and Study Range 23
- 2.6 Convergence 25
  - 2.6.1 Grid Convergence 26
  - 2.6.2 Geometric Convergence 26
  - 2.6.3 Boundary Placement Convergence 28
- 2.7 Validation 29
  - 2.7.1 Low Reynolds Number Validation 29
  - 2.7.2 High Reynolds Number Validation 33
- 2.8 Curve-Fitting 34

3 Results **36**
- 3.1 Introduction 36
- 3.2 Simulation Results 36
- 3.3 Grid Convergence 39
- 3.4 Geometric Convergence 42
- 3.5 Boundary Placement Convergence 44
- 3.6 Validation 48

3.7 Curve-Fitting 50
3.8 Flow Field Visualization 54

4 Discussion 59
4.1 Model Accuracy 59
4.1.1 Convergence Studies 59
4.1.2 Validation 65
4.2 Model Results 67
4.3 Physical Applicability 73
4.4 Extension of Work 74

5 Summary 76

Bibliography 80

A Blasius Boundary Layer Simulations 83

B Code 86

List of Tables

2.1 Experimental values of lift for a sphere 34

List of Figures

1.1	A schematic displaying the geometry and flow configuration	2
1.2	Photograph of realistic aerosol particles	4
1.3	Free-body diagram of a sphere or cylinder attached to a realistic surface	5
2.1	A schematic of the computational domain for a spherical particle	21
2.2	Computational approximation to actual geometry	28
3.1	Coefficient of lift simulation data points for a sphere	37
3.2	Coefficient of drag simulation data points for a sphere	38
3.3	Coefficient of lift simulation data points for a cylinder	38
3.4	Coefficient of drag simulation data points for a sphere	39
3.5	Grid convergence study for a sphere at a Reynolds number of 1	41
3.6	Grid convergence study for a cylinder at a Reynolds number of 1	41
3.7	Geometric convergence results for a sphere	43
3.8	Geometric convergence results for a cylinder	43
3.9	Boundary convergence results for a sphere Re = 0.1	45
3.10	Boundary convergence results for a sphere Re = 10	46
3.11	Boundary convergence results for a sphere at Re = 250	46
3.12	Boundary convergence results for a cylinder at Re = 0.1	47
3.13	Boundary convergence results for a cylinder at Re = 10	47

3.14 Boundary convergence results for a cylinder at Re = 49 48

3.15 Difference between the simulated drag force (actual) and the analytic drag force for a sphere 52

3.16 Absolute relative error between the curve-fitted functions for lift and drag and the simulated values for a sphere 53

3.17 Difference between the simulated drag force (actual) and the analytic drag force for a cylinder 53

3.18 Absolute relative error between the curve-fitted functions for lift and drag and the simulated values for a cylinder 54

3.19 Contour plot of velocity field at $Re_{cylinder} = 0.06$ 55

3.20 Streamline plot of velocity field at $Re_{cylinder} = 0.06$ 55

3.21 Contour plot of velocity field at $Re_{cylinder} = 49$ 56

3.22 Streamline plot of velocity field at $Re_{cylinder} = 49$ 56

3.23 Contour plot of velocity field at $Re_{sphere} = 0.1$ 57

3.24 Streamline plot of velocity field at $Re_{sphere} = 0.1$ 57

3.25 Contour plot of velocity field at $Re_{sphere} = 250$ 58

3.26 Streamline plot of velocity field at $Re_{sphere} = 250$ 58

4.1 Variation of lift coefficient for a sphere in the Reynolds number range 0.1 – 250 70

4.2 Variation of drag coefficient for a sphere in the Reynolds number range 0.1 – 250 70

4.3 Variation of lift coefficient for a circular in the Reynolds number range 0.06 – 49 71

4.4 Variation of drag coefficient for a sphere in the Reynolds number range 0.06 – 49 71

4.5 Velocity profile variation with plate Reynolds number, $Re_{cylinder} = 250$ 72

4.6 Velocity profile variation with plate Reynolds number, $Re_{sphere} = 250$ 72

Chapter 1

Introduction

In fluid dynamics, two of the most widely examined external flows are the flow around a sphere, as well as its two dimensional counterpart, flow around a circular cylinder. The flow around a spherical body has been well studied partly because of its orientation-nonspecific geometry and consequent simplicity, but also from the physical relevance of this geometry. Experimental, computational, and analytical methods have yielded many results for varied flow conditions. A sphere in a uniform flow is an example of a straightforward problem from which much information can be extracted, such as dimensionless relationships between the coefficient of drag, Reynolds number, and surface roughness, the Reynolds number at which the Navier-Stokes equations are nearly linear, the Reynolds number at which the flow becomes unsteady, the relationship between hairpin vortex shedding frequency and other dimensionless parameters, the Reynolds number at which turbulent flow develops, insight into boundary layers, and a host of other interesting

information.[1,2,3] The solutions to these inquiries have been gained over many decades, and just as science should, the results have yielded not only a better understanding of nature, but a host of new problems.

The present research adds to the body of knowledge concerning flow about a sphere and a circular cylinder. Specifically, numerical analysis was used to examine laminar, steady flow about a sphere attached to a planar, flat wall when the external flow is a fully-developed Blasius boundary layer. Additionally, the 2-dimensional equivalent of the spherical problem was examined, which is an infinite circular cylinder attached to a planar wall. A schematic of the problem is shown in Figure 1.1. The objective of this work is to obtain empirical relationships that can be utilized to calculate the lift and drag forces acting on a sphere or cylinder attached to a plane over which flows a Blasius boundary layer.

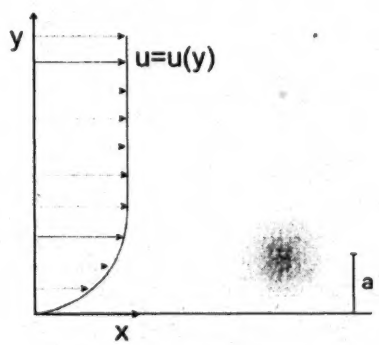

Figure 1.1: A schematic displaying the geometry and flow configuration examined in the present research. The velocity profile u(y) is a fully-developed Blasius boundary layer. The obstacle is a sphere or cylinder of radius a.

1.1 Background

An approximately spherical particle attached to a nearly planar surface with a fluid flowing parallel to the wall occurs in many situations. Examples include sediment on a riverbed, pollen in a boundary layer, contaminant particle removal in microfabrication, or entrance duct flow with dust particles adhering to the surfaces.[4,5,6] An example of a cylinder attached to a wall in a boundary layer is a pipeline in an atmospheric boundary layer.[7]

The applications which spurred this work exist in the field of pharmaceutical aerosols. A class of pharmaceutical aerosol that is gaining in popularity is the dry powder inhaler.[8,9] Small ($\prec$ 10 μm), drug-laden, roughly spherical particles are delivered to a patient's respiratory tract when air is inhaled through the device which contains the particles. The particles may or may not migrate into the patient's air stream depending on the aerodynamic forces on the particles. Powder particles produced from a spray-freeze-drying manufacturing method are shown in Figure 1.2, which demonstrates that a spherical geometric approximation is appropriate. It should be noted that the surface roughness will alter the flow field and aerodynamic force predictions. A necessary function of the inhaler is to generate the flow conditions required to entrain the powder particles from a blister packet or powder storage area into the patient's inhalational flow. A boundary layer develops in the inhaler and over the bed of particles. The first step in predicting if the particles will

aerosolize is to understand the aerodynamic forces on individual, idealized particles. This work is aimed at achieving that goal for a simple boundary layer flow.

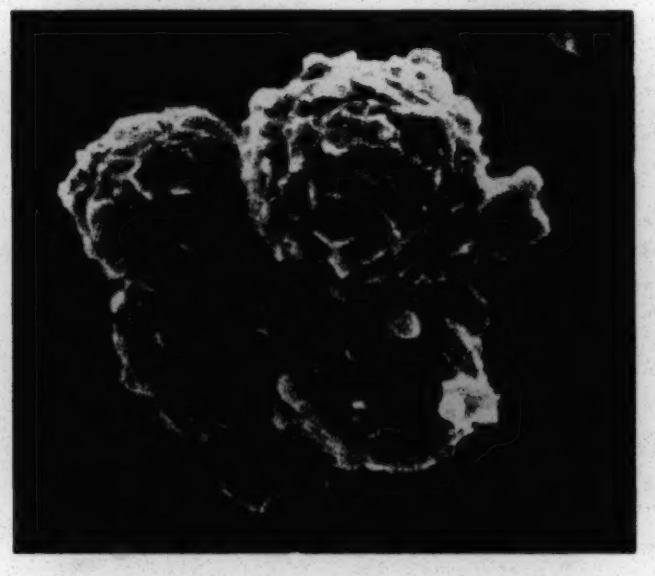

Figure 1.2: An agglomeration of powder particles from a pharmaceutical application produced using spray-freeze-drying that show an approximately spherical geometry.

In general, knowledge of the forces on a sphere or cylinder attached to a wall in a Blasius boundary layer allows more accurate and wide-ranging impending motion models to be developed. Figure 1.3 shows a particle, which could be spherical or cylindrical, attached to a realistic wall. Complete knowledge of the forces and geometry as well as the dynamics (if the particle is rocking about an asperity) allow accurate prediction of the particle acceleration, whether it be by vertical motion, rolling, slipping, or some

combination. The forces in a generalized model include: electrostatic forces (electric double-layer, if aqueous, and van der Waals), weight, contact force, friction, drag, lift, and possible mechanical force (if the particle is attached to the wall, as occurs in micromachining applications). Electrostatic forces can and have been characterized using a centrifugal test and/or atomic force microscopy.[10,11] Aerodynamic forces have been analysed for very few external flows that are relevant in this context, and only under specific circumstances (typically very low Reynolds number).

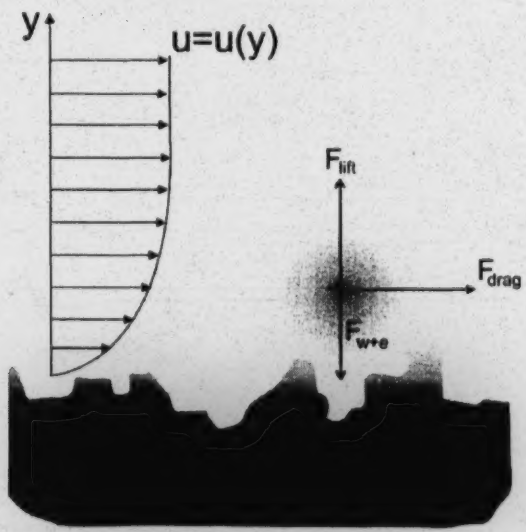

Figure 1.3: Schematic representing a sphere or cylinder on a real surface. The forces acting on the body are hydrodynamic (lift and drag) and particle weight, and electrostatic forces. Contact and friction forces are omitted for clarity.

A variety of models exist that predict spherical particle entrainment rates for a turbulent boundary layer.[12] These models assume that the particles

are small enough in diameter to exist in the viscous sublayer of a turbulent boundary layer and use either analytical results from laminar shear flow about a free sphere or experimental relationships for predicting the aerodynamic forces. To the author's knowledge, no particle entrainment model exists solely for predicting particle movement in a laminar flow situation nor do models exist that predict cylindrical body entrainment in any type of boundary layer. The results from this research could be used in the creation of such a model. The primary applicability of this research is in impending motion models of particles attached to a wall in a boundary layer.

1.2 History

Currently, all analytical solutions for flow about a sphere attached to a wall consider the velocity profile to be a linear shear flow, and the Reynolds number of the sphere to be low enough to neglect the non-linear convective terms in the Navier-Stokes equations. This is an acceptable approximation to small spheres in many flow profiles, but has serious accuracy limitations when the flow curvature is non-negligible. Saffman derived a celebrated result for lift on a spherical particle in shear flow.[13] However, it is known that the accuracy of the result is greatly compromised when the sphere approaches a wall. Cherukat and McLaughlin extended the analysis to include the effects of a wall.[14] O'Neill analysed the drag force on a sphere attached to a wall in shear flow at low Reynolds number, but did not obtain a result for the

coefficient of lift.[15] The problem was revisited by Leighton and Acrivos who included first order inertia effects in a perturbation analysis to obtain a lift result.[16] The generalized results of Cherukat and McLaughlin decompose to the lift result first presented by Leighton and Acrivos when the sphere touches the plane. Shear flow analyses are important because, as sphere diameter decreases, many laminar flows appear to be shear flows (e.g. viscous sublayer of a turbulent boundary layer, Poiseuille flow). However, as the sphere diameter increases, the relationships become less accurate.

Experiments in mineral oil were completed by Willets and Naddeh (1987) who examined the lift force on a sphere in a laminar boundary layer and the force variation with perpendicular distance from the wall.[17] They presented results for a sphere Reynolds number of ~ 100. A low sphere Reynolds experiment (~0.1) in shear flow was recently reported which utilized methods from atomic force microscopy to examine both lift and drag on a sphere touching a wall.[18] The technique admittedly needs refinement to achieve results with substantial accuracy. To the author's knowledge, there exist no experimental results for the coefficient of drag with laminar flow in the present geometry at high sphere Reynolds numbers.

Laminar to turbulent boundary layer transition induced by a spherical roughness element was examined by Mochizuki.[19,20] Smoke from paraffin and stereographic photography were used to examine the various flow regimes. At low velocities, and sphere Reynolds number (Re~250), a steady horseshoe

vortex was observed about the sphere as well as a pair of trailing vortices that originate in the wake of the sphere. As the velocity was increased, the trailing vortices become unsteady and oscillate. Upon further increase in fluid velocity, the slight oscillations in the trailing vortices are transformed to hairpin vortices, which are shed behind the sphere in a periodic manner. The horseshoe vortex is close to the wall and steady at low Reynolds number (Re~250), but becomes unsteady when the trailing vortices become unsteady. Increased fluid velocity causes the flow about the sphere to become turbulent.

Curiously enough, there exist no analytical results for the case of creeping shear flow past a cylinder attached to a plane surface. Additionally, there are no experimental results for lift and drag forces on a cylinder in low Reynolds number flow and there is no experimental or computational evidence that indicates at which Reynolds number the flow about the cylinder becomes unsteady. To be sure, the cylindrical geometry has been examined experimentally in a boundary layer, but often the boundary layer is turbulent and the Reynolds number of the cylinder is of the order 10000.[21,22] The experimentalists are almost exclusively interested in the changes and/or suppression of vortex shedding due to the presence of the boundary layer and plane wall.

1.3 Computation

The solution of a fluid flow problem involves two broad stages. The first is selecting an appropriate mathematical model to characterize the problem of interest, and the second is exploiting analytical or computational methods to solve the problem. In this research, a commercially available computational package, ANSYS CFX, was utilized to solve the Navier-Stokes equations for laminar flow about a sphere and cylinder attached to a wall.

Paramount to any computational study is determining the source of error and uncertainty and controlling or minimizing it. The terms verification and validation arise often when using computational methods in fluid mechanics. Broadly, validation is a demonstration that the physical model matches reality, and verification is determining how reliably and accurately the computational code solves the physical model under consideration.[23] Validation of a computational model is achieved through comparison of numerical results to accurate and reliable experimental measurements. Verification of a model involves examining a variety of sources of error, primarily discretization error. The following list outlines the errors typically examined in verification of a model.[24]

- Discretization error: an error arising from the transformation of differential or integral operators to algebraic relationships.

- Iteration error: an error arising from the iterative, inexact solution of the set of algebraic equations.
- Round-off error: an error that arises in conjunction with iteration error. It is inexact electronic algebraic operations arising from the limited precision of a computer.
- User errors: errors that occur from the neglect or inattention of a user.
- Code errors: programming mistakes.
- Model error/uncertainty: the error associate with imprecise knowledge of boundary conditions as well as errors in boundary condition implementation and placement, approximation or inadequate knowledge of the geometry being modeled, and sometimes inaccurate knowledge of fluid properties.

Both verification and validation were utilised in this research to ensure accurate, credible, and physically applicable results.

1.4 Summary of Thesis

A detailed explanation of the theory and methods of this work is presented in Chapter 2. Specifically, information is given on the precise mathematical models solved, the method of solution, and the method for checking accuracy. Chapter 3 presents the solution results, and a discussion is followed in Chapter 4. Chapter 5 gives an overview of the work.

The appendices include preliminary boundary layer numerical studies and auxiliary computer programs, such as a Blasius equation solver and curve-fitting program, used in this research.

Chapter 2

Methods and Theory

2.1 Introduction

The objective of this research is to develop relationships that can be utilized to predict the lift and drag forces on a sphere attached to a wall in a fully-developed Blasius boundary layer. A cylinder attached to a wall oriented perpendicular to the free-stream direction is also examined. This chapter discusses the methods utilized to produce those results, including the mathematical models and numerical method used.

2.2 Mathematical Models

The Navier-Stokes equations and continuity, coming from the conservation of linear momentum and mass, are the physical models utilized in this research. Beyond assuming the fluid being modeled is a continuous medium, the primary assumption used to generate the Navier-Stokes equations is that the fluid is Newtonian. A Newtonian fluid demonstrates a linear relationship between viscous stress tensor and the strain rate tensor. This is the

simplest friction law, outside of assuming negligible friction, that can be implemented. Additionally, the fluid is assumed to be isotropic. The Newtonian model has proved to be a reliable and well-used model for the most common fluids under most conditions. In this research, the fluid is assumed incompressible and the viscosity is assumed constant. This limits the applicability of the results to subsonic flow and flow with negligible temperature gradients. Furthermore, unsteady effects are not examined in this research. The resulting equations are:

Mass conservation: $$div(\mathbf{u}) = 0 \quad (1)$$

Momentum conservation: $$\rho(\mathbf{u}\cdot\nabla)\mathbf{u} = \rho\mathbf{g} - \nabla p + \mu\nabla^2\mathbf{u} \quad (2)$$

Where ρ is pressure, **u** is the velocity vector, μ is the dynamic viscosity and **g** is the gravitational constant in vector form.

The equations are often non-dimensionalized prior to numerical solution to produce generalized results. However, an alternative method is to solve the dimensional form of the equations and non-dimensionalize the results, similar to experimental fluid dynamics. The latter method was adopted in this work.

2.3 Numerical Method and Grid Generation

2.3.1 Discretization

The numerical method adopted in this research is the control volume technique, where the conservation laws are used in their integral form, assuming steady state.[25] The governing equations are then as follows.

Mass conservation: $$\int_S U_j dn_j = 0 \qquad (3)$$

Momentum conservation: $$\int_S \rho U_j U_i dn_j = -\int_S P dn_j + \int_S \mu \left(\frac{\partial U_i}{\partial x_j} + \frac{\partial U_j}{\partial x_i} \right) dn_j \qquad (4)$$

All integrals are surface integrals and dn_j represents the outward normal vectors of the surfaces. The commercial software utilized for this research uses a single cell, co-located grid for variable storage and calculation. All variable information is stored at nodal locations.

An important component of an incompressible Navier-Stokes solver is the method by which the pressure and velocity fields are coupled. A Poisson equation is typically derived by taking the divergence of the momentum equation and simplifying the resulting equation with the continuity relationship. In this way, a velocity field is generated through the solution of the momentum equations. The velocity field is updated, and forced to obey continuity, by solving the Poisson equation for the pressure field. This method is the framework for the SIMPLE family of pressure-velocity coupling. The commercial package used in this research uses a method based upon the work of Rhie and Chow.[26] A fourth-order pressure derivative is added to continuity to distribute the pressure influence. The continuity equation remains consistent despite this modification because a third-order grid spacing term is multiplied by the pressure derivative. Hence, the inconsistent term approaches zero as the

grid is refined. The first-order derivatives are discretized using a second-order central difference approximation.

Velocity and pressure field data as well as other variational quantities (temperature, density, concentration, etc.) are stored at nodal points (co-located). To determine a variable value at a point in an element other than at a node, interpolation with shape functions is used. The shape functions are parameterized with a local coordinate system attached to a given element, and vary linearly with these parameters. The formulas used for interpolation are as follows, where ϕ is the variable under consideration.

$$\phi = \sum_{i=1}^{N_{node}} N_i \phi_i \tag{5}$$

where N_i is parameterized in terms of a local coordinate system attached to each element.

The pressure gradient term is calculated as the linearly interpolated pressure value multiplied by the area of the volume face under consideration. The diffusion term is slightly more difficult to discretize, but the accuracy of both the pressure and diffusion terms is determined by the interpolation scheme.

The nonlinear advection term is the most difficult term to discretize and there are three options within the computational software used. The upwind difference scheme is a well-known, first-order accurate option that provides

stable solutions, but suffers from the large amount of numerical or artificial diffusion it generates in the solution.

$$\text{Upwind:} \qquad \phi = \phi_{upwind} \tag{6}$$

A second-order central difference scheme can be utilized, and is produced by interpolating from the values at surrounding nodes to obtain variable under consideration. The software manufacturer recommends against using this discretization due to issues of pressure-velocity decoupling.

The convective discretization used in this research is based on the upwind scheme with a corrective factor.

$$\phi = \phi_{upwind} + \beta \nabla \phi \cdot \mathbf{r} \tag{7}$$

where **r** is the vector from the upwind node to the integration location under consideration. If the constant β is set to unity, the discretization is second-order accurate. However, in order to increase stability, the value of β is allowed to vary within the domain during the solution. At points in the domain where the gradient of the variable ϕ is small the β is forced to approach zero so that the scheme becomes upwind. Otherwise, the value of β is calculated to be as close to unity as possible. The algorithm used to calculate β is based on the work of Barth and Jesperson.[27]

2.3.2 Algebraic Solution of Discretized Equations

The set of non-linear equations obtained from the finite volume are solved simultaneously and iteratively using the incomplete lower/upper

factorization technique. In addition, an algebraic multigrid method, additive correction, is used to enhance convergence rate. In steady state simulations, false time-stepping is used to generate a solution.

The accuracy to which the system of linear equations is solved is monitored through normalized residuals. The raw residual for a given variable or quantity for a given finite volume is a measure of imbalance in a conservation equation for a given volume. It is normalized through representative variable and coefficient values.

In this work, the residuals monitored were mass and the three components of momentum. The solution of the linear equations was deemed complete when the normalized residuals, mass and the three momentum quantities, reached a steady value with respect to iteration level.

2.3.3 Mesh Generation

The mesh is generated in two steps. First, a 2-dimensional surface mesh is created on the domain faces using a Delaunay Surface Mesher. Subsequently, the surface mesh is used to produce the volume elements using an advancing front technique. Tetrahedral and prism elements are used in the meshing process. The prism elements are high aspect ratio elements which are used to resolve the wall-normal velocity gradients in a boundary layer while maintaining a coarse streamwise resolution. The majority of the domain was

filled with tetrahedral elements. Grid information was stored in double-precision format.

2.3.4 Force Calculation

The general force on a surface is given by Eqn. 8.

$$F_n = \iint_S \{p\mathbf{n}\cdot\mathbf{n}_s + \boldsymbol{\tau}\cdot\mathbf{n}\}dA \qquad (8)$$

Where $\mathbf{n}$ is the unit vector designating the direction of the force and $\mathbf{n}_s$ is the surface unit normal vector of the sphere surface, S. The shear stress and pressure are represented by the terms τ and p, respectively. In this research, the lift and drag forces acting on the sphere surface are calculated by replacing $\mathbf{n}$ with the vectors <0,0,1> and <0,1,0>, correspondingly The pressure and shear terms are calculated and outputted in the solution stage of the problem.

2.4 Boundary Conditions

Correct choice of boundary conditions and their placement plays an important role in numerical studies. There are three basic categories of boundary conditions available for use with a system of partial differential equations: Neumann, Drichlet, or mixed. The appropriate choice of boundary condition for a particular location depends upon the physical system being modeled and also on the nature of the partial differential equation (or system of equations); whether they are elliptic, hyperbolic, or parabolic, and where their characteristic lines run. However, the Navier-Stokes equations are nonlinear

due to the convection terms, and such linear analysis holds under simplifying assumptions (Stokes flow, high Reynolds number flow, etc.). One such flow is boundary layer flow, which is parabolic with the characteristic line being the streamwise direction. In this equation, an outlet boundary condition is not needed as the solution can be marched forward in space; upwind solutions are solely dependent on the downwind conditions. Placing a spherical or cylindrical obstacle in the boundary layer possibly invalidates the parabolic characterization of the defining partial differential equations. Hence, determining the boundary conditions necessary for a well-posed problem becomes problematic. The computational code used in this research places boundary conditions on every boundary, which potentially leads to an overdetermined system of equations, such as the case with laminar boundary layer flow without the spherical obstacle present. However, the program produces correct Blasius boundary layer predictions, even when the system is overdetermined (Appendix A). The offending boundary condition is an opening-type boundary condition; one that allows flow into and out of the domain. This type of boundary condition remains incompletely understood, and it seems that in some situations, by converting a system of partial differential equations to a nonlinear system of algebraic equations a degree of rigidity in the well-posedness of a problem is lost.[28] Viable numerical solutions can be achieved for seemingly ill-posed mathematical problems.

Reference 28 conjectures that the open boundary condition works due to truncation effects, but more research is needed in this regard.

The computational domain is shown in Figure 2.1. The surface of the sphere as well as the wall utilize the no-slip boundary condition, as follows.

$$u, v, w = 0 \tag{9}$$

The inlet utilized a fully-developed Blasius velocity profile. The Reynolds number with respect to plate length at the location of the sphere was kept constant throughout the study at a value of 32 400. This is sufficiently greater than the minimum fully-developed constraint of $Re_x > 1000$ and is also well beneath the turbulent transition Reynolds number of 3 000 000.[29] The remaining boundaries are nonphysical and numeric approximations. The analytical boundary condition for the top boundary, Eqn (10), can only be implemented exactly by transforming the domain so as to have infinite boundary placement possible. As is most often the case, Eqn (10) is approximated by placing the boundary at some finite distance and testing the influence of its placement on the solution. The latter method was adopted in this research. It is unclear what the analytical boundary conditions should be on the two remaining opening boundaries. However, the ideal numerical scheme should have some features, including allowing passive inflow/outflow along with anything the flow carries (e.g. prevents non-physical reflection of waves), and most importantly they would produce identical solutions in the computational domain for any boundary placement[28].

$$\mathbf{u} = U \ \ at \ z = \infty \tag{10}$$

All openings in the domain shown in Figure 2.1 are treated with the following boundary conditions:

$$\frac{\partial \mathbf{u}}{\partial \mathbf{n}} = 0$$
$$P_{opening} = P_{specified} = 0 \tag{11}$$

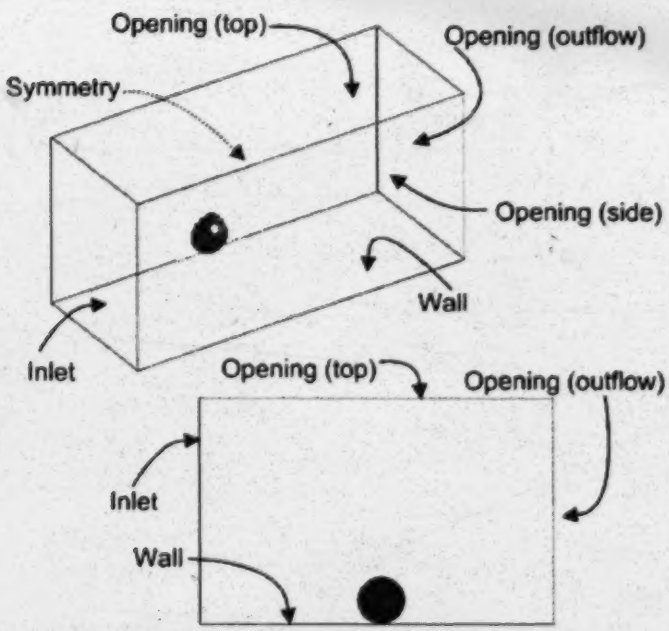

Figure 2.1 A schematic showing the computational domains utilized to model a spherical particle and a cylindrical particle attached to a wall. The domains utilize opening-type boundaries, a symmetry boundary, an inlet, the sphere surface and the wall.

The specified pressure is taken to be relative to total pressure when the flow is into the domain and relative to static pressure when the flow is out of the domain. The no-slip boundary conditions as well as the prescribed velocity

profile at the inlet are exact boundary conditions. The boundary conditions displayed in Eqn (11) are widely used and mostly successful; however, they do not satisfy the ideal opening boundary traits. Boundary placement influences the solution in the domain. As outlined in Reference 28, the disturbance to the domain is typically localized near the opening.

If one were to take a Blasius boundary layer and slice it with an imaginary plane perpendicular to both the stream wise direction and the wall, the streamlines never achieve zero slope in the range $0 \le \delta < \infty$; the velocity slope is non-zero everywhere and varies with distance. This is evidence enough that the boundary conditions are not physical, but can they produce accurate results? Since the boundary layer equations are parabolic, the outlet boundary conditions need not exist; and consequently the error in the boundary conditions is confined to an area near the boundary. This was examined and confirmed in preliminary boundary layer simulations (without the presence of a sphere), and the results are shown in Appendix A.

Boundary conditions that are more physical would allow streamline slope at the opening boundary to vary across the boundary. This could be implemented with a higher order normal derivative, as shown in Eqn (12).

$$\frac{\partial'' \mathbf{u}}{\partial \mathbf{n}''} = 0 \qquad (12)$$

This option was not available for use in the commercial code utilized for this research.

2.5 Dimensional Analysis & Study Range

A sphere in a general, not necessarily similar, boundary layer has coefficients of lift and drag that are functions of sphere Reynolds number and the ratio of sphere diameter to boundary layer thickness, as well as the ratio of sphere diameter to height above the surface. An example would be a sphere in the developing stages of a Blasius boundary layer, where the coefficients of lift and drag could be expected to be functions of both the sphere Reynolds number and the plate Reynolds number. In this study, the ratio of sphere diameter to height is specified. Also, in a Blasius boundary layer the boundary layer thickness is dependent upon the Reynolds number with respect to plate length. Consequently, the sphere diameter to boundary layer thickness ratio can be replaced with the Reynolds number of the plate length. The Reynolds numbers are defined as follows:

$$\begin{aligned} \mathrm{Re}_{sphere} &= \frac{\rho U_{\phi/2}\phi}{\mu} \\ \mathrm{Re}_{x} &= \frac{\rho U_{\inf} x}{\mu} \end{aligned} \qquad (13)$$

Here $U_{\phi/2}$ is the velocity in the boundary layer absent of a sphere at a height of half a sphere diameter, $\phi/2$, x is the location along the plate at which the sphere is located and U_{inf} is the freestream velocity. The aerodynamic force coefficients are functions of Reynolds numbers described in Eqn. (13):

$$\begin{aligned} C_L &= f(\mathrm{Re}_{sphere}, \mathrm{Re}_x) \\ C_D &= g(\mathrm{Re}_{sphere}, \mathrm{Re}_x) \end{aligned} \qquad (14)$$

A cylinder attached to a wall is complicated by the fact that the lift and drag relationships are not independent of cylinder orientation. However, in this study the cylinder orientation is specified as perpendicular to the freestream direction and parallel to the wall. In this research the Reynolds number with respect to plate length is set at an intermediate value, 32 400. Under this constraint, the objective of this research was to determine the single-variable functional relationships for f and g.

The first aspect of the study is to specify the range of sphere Reynolds number for simulation. At the low Reynolds number end of the spectrum, the study is bounded by analytical results valid at $Re_{sphere} \rightarrow 0$. Determining the upper bound in Reynolds number is more challenging. This study is concerned with steady, laminar flow about a sphere attached to a wall in a fully-developed Blasius boundary layer. To determine the upper bound is to find the sphere Reynolds number at which hairpin vorticies start shedding. This can be accomplished numerically at great cost and questionable accuracy, but is better determined from experimental results. Mochizuki examined the influence a spherical roughness element had on boundary layer transition through smoke wire visualization.[18,19] From that work, the transition from steady to unsteady flow about a sphere is clear; however, sphere Reynolds numbers for various flow regimes were not explicitly reported nor were the fluid transport properties. Assuming air properties at standard condition, the sphere transitioned from steady to unsteady flow at a sphere Reynolds number of 250.

It should be noted that the transitional particle Reynolds number is likely dependent upon the diameter to boundary layer thickness ratio; however, this effect is not examined in this work. The upper Reynolds number bound of the study is considered to be $Re_{sphere} = 250$.

Few analytical and experimental results exist for a cylinder attached to a wall in a Blasius boundary layer. It is not known at what Reynolds number the flow about the cylinder becomes unsteady, so the upper Reynolds number limit was selected as the Reynolds number at which the flow about a cylinder in uniform flow far from a wall becomes unsteady, which is approximately 50.[30] The presence of the wall inhibits the onset of unsteady flow, as seen with the sphere for which unsteadiness is delayed from a Reynolds number of 130 for uniform flow to ~ 250 when attached to the wall. The inhibiting effect of the wall was also observed for Poiseuille flow, where unsteady flow was delayed from a Reynolds number of 75 to 250 when the sphere was placed at the wall compared to at the symmetry plane.[31] Hence, choosing the upper Reynolds number of the cylinder study to be the Reynolds number at which the cylinder undergoes steady to unsteady transition in uniform flow likely ensures steady flow about the cylinder when attached to a wall in a Blasius boundary layer.

2.6 Convergence

An important aspect of any numerical study is determining the influence of the various sources of error, as stated in section 1.3, on the accuracy of the

solution. In this research, the leading source of error arises from inexact boundary conditions, approximated geometry, and discretization error. Three convergence studies were undertaken to characterize and band the errors, consisting of a grid convergence, geometry convergence, and boundary placement convergence studies.

2.6.1 Grid Convergence

The discretization scheme used to convert the Navier-Stokes equations to a system of nonlinear algebraic equations attempts to treat the majority of the domain with a second-order scheme. A coarse grid will produce significant discretization error, and refinement should reduce this error in a nearly second-order fashion. Two simulations were run at each sphere Reynolds number data point to determine if grid convergence had been met. A change in lift or drag coefficient less than 3% was deemed grid convergent when the number of nodes was increased by 50% or more. In addition, at a sphere Reynolds number of 1, a detailed, systematic grid convergence study was completed.

2.6.2 Geometric Convergence

The modeling of a perfectly rigid sphere on a perfectly flat wall involves contact at a single point. This geometric configuration presents great difficulty in the grid generation stage of numerical simulation. The two outcomes of meshing such geometry are either grid generation failure or acceptance of poor quality grid elements (high aspect ratio, low/high internal

angles). To overcome this issue, the geometry at the point where the sphere or cylinder contacts the wall must be changed. The two methods available to modify the contact point geometry are presented in Figure 2.2. In both cases, as $x \rightarrow 0$ the computational geometry approaches the analytical geometry. In this study the case on the left was chosen as the modifying technique, as it does not shift the entire geometry vertically in the velocity gradient. The influence of geometry modification is expected to be related to the ratio of x to ϕ; at some small finite value of the ratio, the coefficients of lift and drag will asymptote to a constant value. This value is the point at which the solution has reached geometric independence. An alternative route to represent the ratio of x to ϕ, in the case of spherical geometry, is to report the ratio of the removed surface area to the total surface area. For the cylindrical, 2-dimensional case, the ratio becomes one truncated perimeter to total perimeter. Analogously, as the area or perimeter truncation ratios approach zero, the computational geometry approaches the analytical geometry. The influence of the area truncation for the sphere was examined at a Reynolds number of 250. The influence of perimeter truncation for the cylinder was examined at a Reynolds number of 49. The truncation area ratio at which the coefficients of lift and drag changed less than 3% was deemed a geometrically converged result.

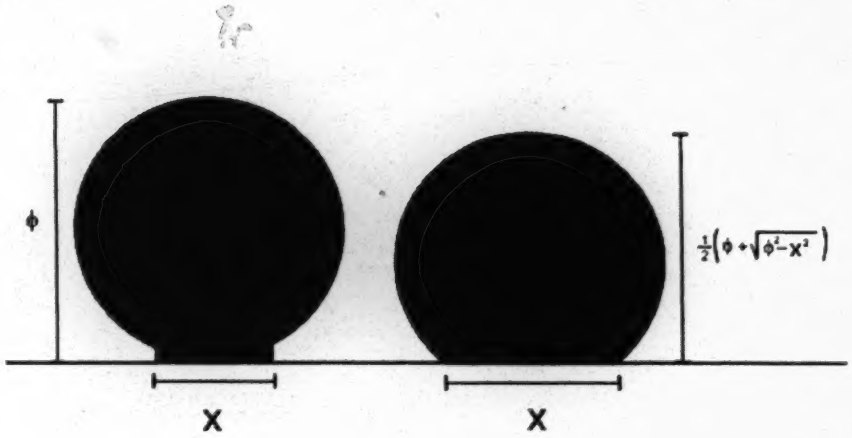

Figure 2.2 Possible modifications to the sphere or cylinder geometry to remove the contact point.

2.6.3 Boundary Placement Convergence

With ideally chosen and implemented boundary conditions, the placement of the boundaries would not affect the solution in the domain. However, given that the opening boundary conditions are inexact, their placement has an effect on the solution. Indeed, even the placement of the inlet boundary condition could alter the solution because the sphere has an upstream influence, which varies with sphere Reynolds number, and the boundary placement may interfere with this upstream influence. In this research, the effect of the placement of the inlet and openings, except for the top boundary, were studied simultaneously at sphere Reynolds numbers of 0.1, 10, and 250, which are the bounding and midpoint Reynolds numbers of the study. The placement of the top boundary was set to fully resolve the boundary layer. At the highest sphere Reynolds number (250), where the ratio of sphere diameter to domain height is highest, the influence of the top

boundary placement was examined. In all cases, boundaries were moved until the coefficients of lift and drag became independent of the placement, displaying successive variation less than 3%.

2.7 Validation

A method to enhance confidence in the results of a numerical study is to compare the calculations at specific, perhaps simplified conditions to available experimental or analytical results. When considering a sphere attached to a wall in a laminar boundary layer, analytical results for lift and drag exist at creeping flow conditions and experimental results for lift are available at high sphere Reynolds number. However, no such experimental or analytical results exist for a cylinder attached to a wall.

2.7.1 Low Reynolds Number Validation

At low sphere Reynolds number, the flow about a sphere attached to a wall takes on the simpler form of shear flow about a sphere, which is a problem that has an analytical solution. Consider the Blasius equation:

$$\begin{aligned} f''' + \frac{1}{2} f f'' &= 0 \\ f &= f(\eta) \\ \eta &= y\sqrt{\frac{U}{\nu x}} \\ f' &= \frac{u}{U} \end{aligned} \qquad (15)$$

with boundary conditions:

$$f(0) = f'(0) = 0$$
$$f'(\infty) = 1 \tag{16}$$

To determine the flow about a sphere at low Reynolds number, consider a series solution to (15) about η=0.

$$f(\eta) = \sum_{0}^{\infty} \frac{f^{(n)}(0)\eta^n}{n!} \tag{17}$$

If the ordinary differential equation in (15) is systematically differentiated with respect to η and the boundary conditions (16) are utilized, the following relationships are obtained.

$$f'(0) = f'''(0) = f^{iv}(0) = f^{vi}(0) = 0$$
$$f^{v}(0) = -f''(0) \tag{18}$$

Substitute these derivative values into the McClaurin series (17) to obtain a relationship valid for small η.

$$f(\eta) = \frac{f''(0)\eta^2}{2} - \frac{f''(0)\eta^5}{120} + O(\eta^{vii}) \tag{19}$$

To determine the stream wise velocity for small η, take the derivative of (19).

$$u = Uf''(0)\eta + UO(\eta^4) \tag{20}$$

The vertical velocity in a boundary layer is nonzero and a relationship can be found through application of the conservation of mass.

$$\frac{v}{U} = \frac{f'\eta - f}{2\sqrt{\mathrm{Re}_x}} \tag{21}$$

The series expansion (19) can be substituted into (21) to obtain a result for vertical velocity in a Blasius boundary layer for small η.

$$\frac{v}{U} = \frac{f''(0)\eta^2 + O(\eta^5)}{4\sqrt{\mathrm{Re}_x}} \tag{22}$$

Since the series solution is valid for $\eta \sim 0$, and also because the Blasius equation comes from the boundary layer equations which are valid for high Reynolds number (Re_x>1000), the stream wise and vertical velocities in a Blasius boundary layer for small η can be written as follows.

$$\begin{aligned} u &= Uf''(0)\eta \\ v &= 0 \end{aligned} \tag{23}$$

Consequently, when considering a sphere at low Reynolds number attached to a wall in a Blasius boundary layer, a velocity field simplification occurs. The problem reduces to linear shear flow about a sphere attached to a wall. O'Neill[15] solved the problem of a sphere attached to a wall in shear flow at low Reynolds number. He first considered the Stokes equation:

$$\begin{aligned} \nabla p &= \mu\nabla^2\mathbf{u} \\ div(\mathbf{u}) &= 0 \end{aligned} \tag{24}$$

O'Neill used the tangent-sphere coordinates as well as Fourier-Bessel transforms to obtain the force on the sphere.

$$\mathbf{F} = (6\pi\mu ua f, 0, 0) \tag{25}$$

Where a is the sphere radius, u is the shear rate, μ is the dynamic viscosity, and f is a dimensionless force coefficient. The value of f was evaluated numerically to be 1.7009. The sphere Reynolds number may be introduced to yield:

$$\mathbf{F} = \left(\frac{1.7009 \cdot 24}{\mathrm{Re}_{sphere}}, 0, 0 \right) \tag{26}$$

The reversibility characteristic of the Stokes equation does not allow for a lift force on the sphere in the analysis. However, vertical migration of spheres in a packed bed was observed experimentally and a Saffman analysis, although incorrect near a wall, predicts a lift force. The analysis of O'Neill thus needs to be expanded to allow lift force at low sphere Reynolds number.

To calculate the lift force, Leighton and Acrivos[16] utilized O'Neill's solution in a perturbation analysis expanding the dimensionless velocity field with respect to Reynolds number. They included first-order inertia effects by expanding the velocity in a series form.

$$\frac{u_i}{\dot{\gamma}a} = \frac{u_i^{(0)}}{\dot{\gamma}a} + \mathrm{Re}\frac{u_i^{(1)}}{\dot{\gamma}a} + o(\mathrm{Re}) \tag{27}$$

Then, upon expressing the lift as a double-integral, and utilizing O'Neill's solution in the integrand, they obtained a result for lift. In dimensional form:

$$L = 9.22(\dot{\gamma}\mu a^2)(\frac{\dot{\gamma}a^2}{\nu}) \tag{28}$$

This can be rendered dimensionless using the definitions of coefficient of lift and sphere Reynolds number to give:

$$C_L = 5.8696 \tag{29}$$

At low sphere Reynolds number, the Blasius velocity profile collapses to the simpler shear flow about a sphere form, whereby the force on a sphere is given as:

$$(C_L, C_D, C_{lateral}) = \left(5.8696, 1.7009 \cdot 24/\mathrm{Re}_{sphere}, 0\right) \qquad (30)$$

Experimental results have been generated for sphere Reynolds number in the range $0.04 < Re < 0.1$ by Muthanna[18] in Poiseuille flow, which at such small Reynolds number represents a linear shear flow about a sphere. The measurement method utilizes apparatus and technique from atomic force microscopy. However, as the author admits, the technique needs further refinement to produce reliable and accurate measurements.

2.7.2 High Reynolds Number Validation

At high Reynolds number, the nonlinear convective terms of the Navier-Stokes' equations contribute greatly to the solution, and make analytical solution prohibitively difficult. In this range, only experimental results exist. Willets and Naddeh[17] examined the lift force on a sphere in a Blasius boundary layer. Specifically, they examined how the lift force varies with gap distance (the ratio of sphere diameter to sphere height off the wall) and the Reynolds number of the sphere and compared the results to predictions from Saffman's analysis. Their results, at a gap ratio of zero, are applicable to this study and are presented in Table 1

Table 2.1 Experimental results for high Reynolds number flow about a sphere attached to a wall in a Blasius boundary layer.

Velocity at Sphere Midpoint (m/s)	Sphere Reynolds Number	Coefficient of Lift	Force (mN)
0.138	43 – 100	0.4	1.009
0.288	83 – 140	0.05	0.552
0.488	140 – 230	0.1	3.173

2.8 Curve-Fitting

The simulation data spans the sphere Reynolds number range $0.1<Re<250$, and the cylinder Reynolds number range $0.06<Re<49$. Exponential functions were chosen as the model curves purely from a visual perspective. Nonlinear regression was utilized to fit the curves to the data utilizing the Gauss-Newton algorithm for optimization. The program starts from an initial guess of the parameters in the curve and calculates the sum of the squares of the vertical error at each point. At the initial guess, a quadratic hyper-surface is generated through a Taylor series expansion to second order terms. The minimum of the quadratic surface is found through equating the gradient of the quadratic function to zero. The Gauss-Newton method estimates the minimum point of the quadratic surface by disregarding the

second order partial derivatives of the function. The resulting estimate of extreme value is utilised as a revised guess for the minimum of the sum of the square of the error. The algorithm is iterated until a specified level of error is reached. The Gauss-Newton method converges rapidly but is strongly dependent on the quality of the initial guess.

The functions fitted to the data for the sphere attached to a wall were forced to match the low Reynolds analytical results. This was achieved with the coefficient of drag by defining the following function.

$$C_D = \frac{C_{D,ana}}{(1 - C_{D,curve})} \tag{31}$$

Where the function $C_{D,curve}$ is fit with an exponential function and tends to zero as the sphere Reynolds number tends to zero. For the coefficient of lift, exponential functions that tended to zero at low Reynolds number were added to the analytical expression for lift coefficient.

Chapter 3

Results

3.1 Introduction

In this chapter, the results of the numerical study are presented. The numerical studies are broken into two main categories: model data and accuracy determination, and are presented in this order. At the end of the chapter, some flow field images are presented.

The model data contains simulations which give accurate prediction of drag and lift variation with sphere Reynolds number at a constant Reynolds number with respect to plate length of 32 400. The model accuracy sections contain convergence studies of geometry, grid refinement, and boundary placement. In addition, the validation of the model predictions to analytical and experimental results is presented.

3.2 Simulation Results

A total of 23 simulations were utilized to capture the variation of coefficient of lift and drag over the Reynolds number range 0.1 – 250 for the

sphere and 16 simulations to cover the cylinder Reynolds number range 0.06 – 49. The simulations used the results from the convergence and accuracy testing to produce accurate data points. Variation of lift and drag coefficient with Reynolds number are displayed in Figures 3.1 and 3.2 for the sphere and Figures 3.3 and 3.4 for the cylinder. In the dimensional model, the inlet velocity profile and sphere or cylinder diameter were varied to change particle Reynolds number. At low Reynolds number, the analytical behavior of the coefficients, for both spherical and cylindrical geometry, can be seen as the coefficient of lift is beginning to asymptote to a constant value and the coefficient of drag displays inverse proportionality to sphere Reynolds number.

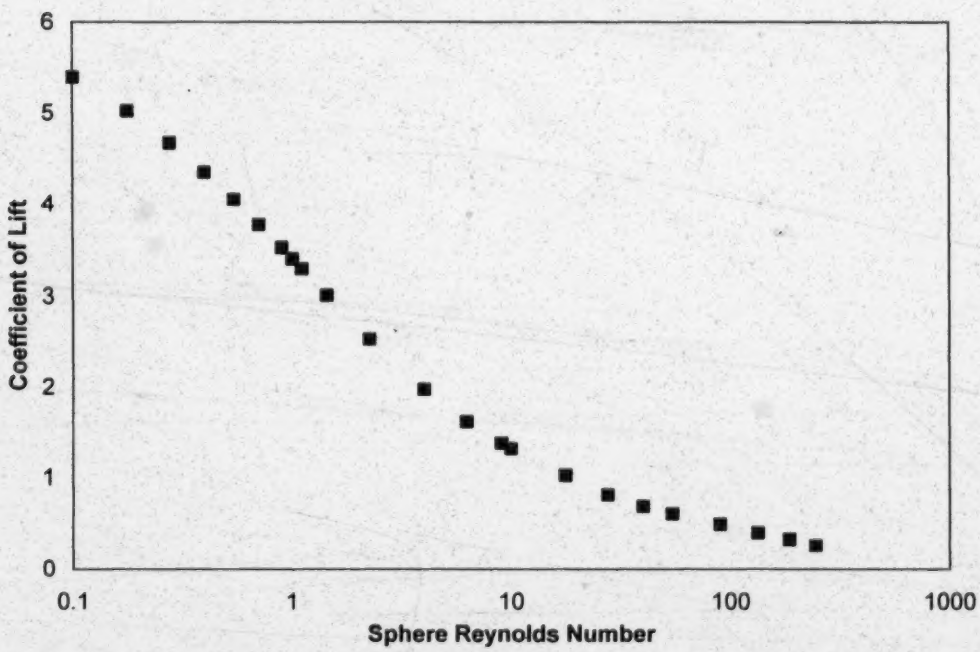

Figure 3.1 Numerical simulation data points displaying the variation of lift coefficient with sphere Reynolds number for the case of a sphere attached to a wall.

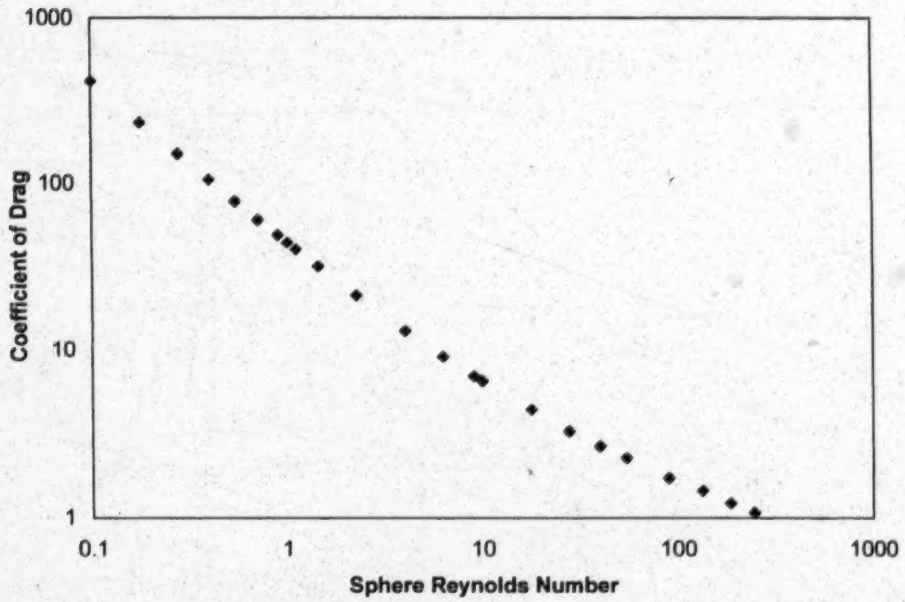

Figure 3.2 Numerical simulation data points showing the variation of drag coefficient with sphere Reynolds number for the case of a sphere attached to a wall.

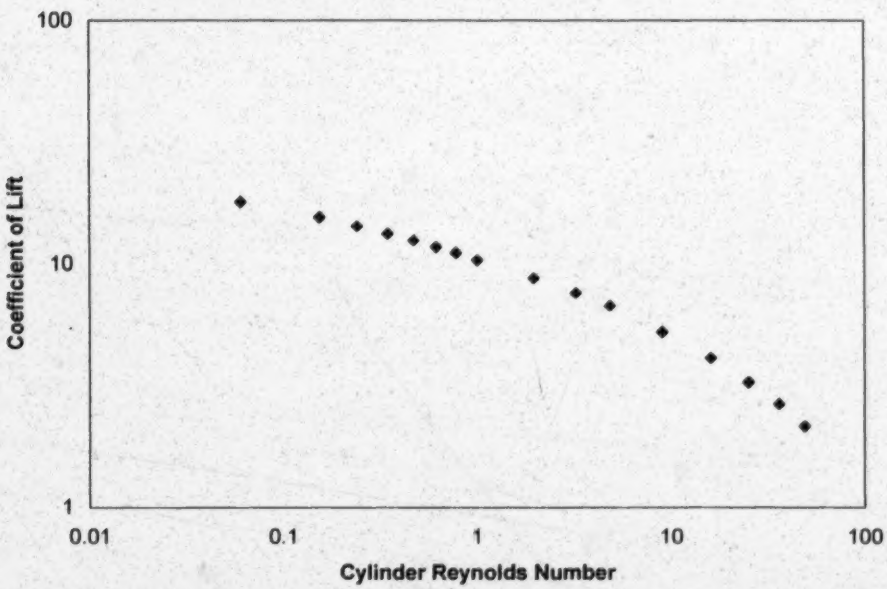

Figure 3.3 Numerical simulation data points showing the variation of lift coefficient with cylinder Reynolds number for the case of a cylinder attached to a wall.

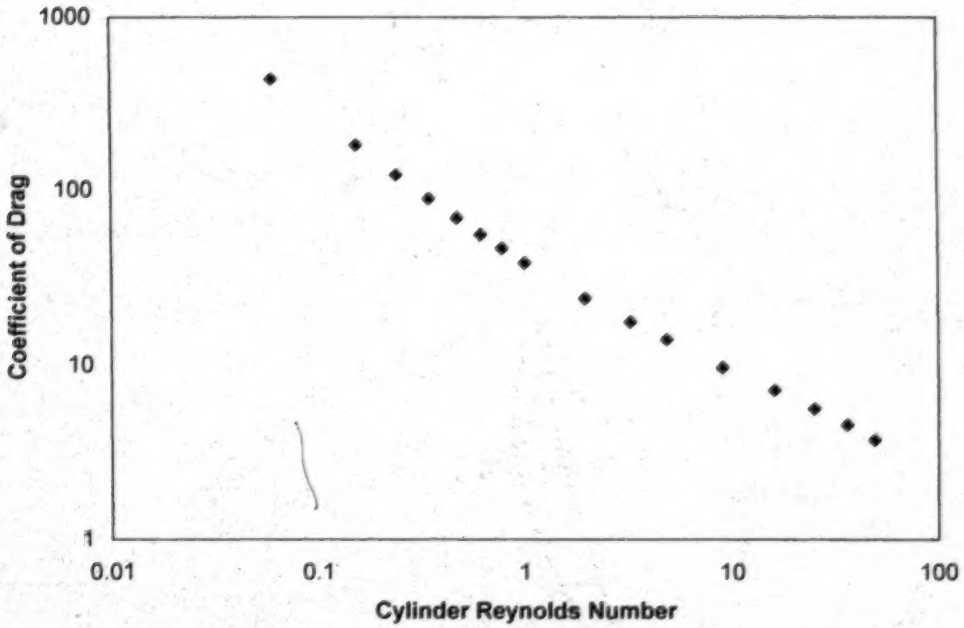

Figure 3.4 Numerical simulation data points showing the variation of drag coefficient with cylinder Reynolds number for the case of a cylinder attached to a wall.

3.3 Grid Convergence

Discretization error is an obvious and conceptually simple error to examine in numerical simulations. It is dependent on the discretization scheme as well as the level of grid refinement. To examine discretization error, different meshes need to be produced to examine the influence level of refinement has on solution variation.

To begin, a boundary layer absent of a sphere and cylinder was simulated at various grid refinement levels to determine the necessary conditions to accurately resolve a Blasius boundary layer. The results are displayed in Appendix A. The integral quantities δ^* and θ reached grid

convergence using 30 – 40 high aspect ratio prismatic elements near the wall. These elements are designed to provide fine mesh resolution perpendicular to the wall, but remain relatively coarse in the streamwise direction. A total of 60 nodes were used to resolve the boundary layer.

For the geometry containing a sphere, at a sphere Reynolds number of 1, a detailed grid convergence study was undertaken. The nodal density was left low at distances far from the wall, but was increased at the wall and about the sphere. Grids were systematically refined while attempting to maintain the relative nodal density variation. The domain for the study had a top far field boundary placement of 30 sphere diameters and all other boundaries were two diameters from the sphere. The influence of the number of nodes, which is equal to the number of control volumes in the discretization, on the coefficients of lift and drag is shown in Figure 3.5. The percent change in coefficient of lift and drag in the most refined simulations is 0.8% and 0.04%, respectively. For the case of a cylinder attached to a wall, the domain under consideration had an equally placed inlet and outlet boundary at 5 cylinder diameters and a domain height of $2*\delta_{99}$. The results of the grid convergence study are presented in Figure 3.6. At the highest level of refinement, the coefficient of lift and drag changed by less than 0.05% and 0.1%, respectively.

Each of the final data points was checked for grid convergence by creating a mesh with ~ 30 – 40% fewer nodes and observing a change in coefficient of lift and drag less than 3 %.

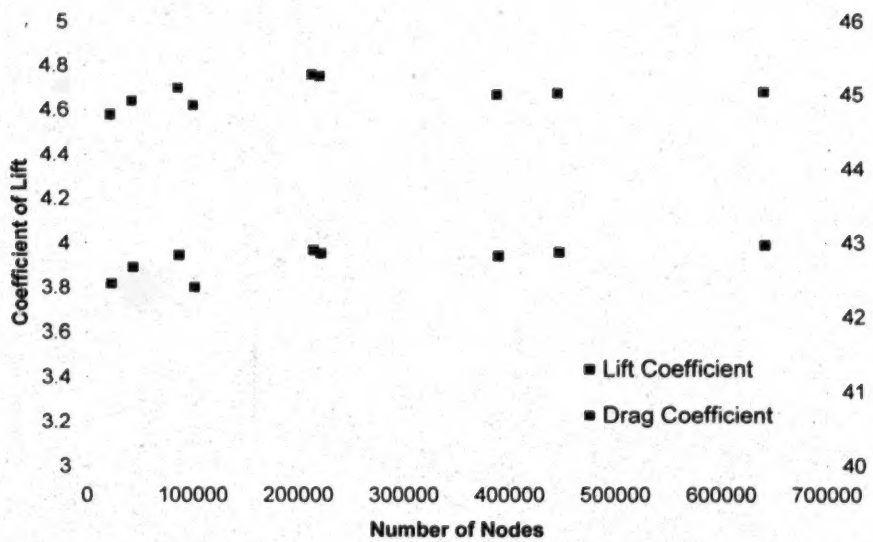

Figure 3.5 Grid convergence study for a sphere attached to a wall at a Reynolds number of 1.

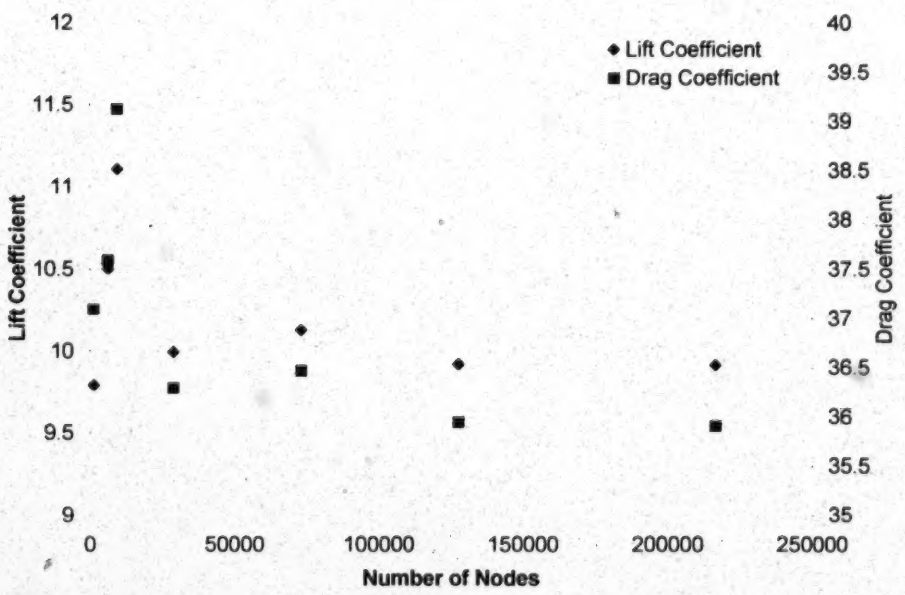

Figure 3.6 Grid convergence study for a cylinder attached to a wall at a Reynolds number of 1.

3.4 Geometric Convergence

A sphere or cylinder contacting a flat surface presents great difficulties for meshing at and near the point of contact. The method adopted in this research to overcome the difficulty is to replace the point of contact with an alternate geometry. In the case of a sphere attached to a wall, a vertical cylinder intersecting the plane and the sphere was utilized. As the cylinder diameter approaches zero, the simulation geometry approaches the true geometric configuration.

At a sphere Reynolds number of 250, the effect of cylinder diameter on the coefficients of lift and drag was examined. The results are reported as a percentage of sphere surface area removed due to the fact that forces are proportional to surface area. Variation of lift and drag with truncation is shown in Figure 3.7. At a truncation below 0.45%, the force coefficient of lift and drag varied less than 1.1 and 2.3%, respectively.

Considering the case of a cylinder attached to a wall in a boundary layer, the point of contact was modified by placing a rectangle at the point of contact. The results are reported as percentage of perimeter removed. The results are presented in Figure 3.8. Increasing the truncation from 3.2% to 4.8% results in lift and drag coefficient changes of 0.07% and 0.14%, respectively.

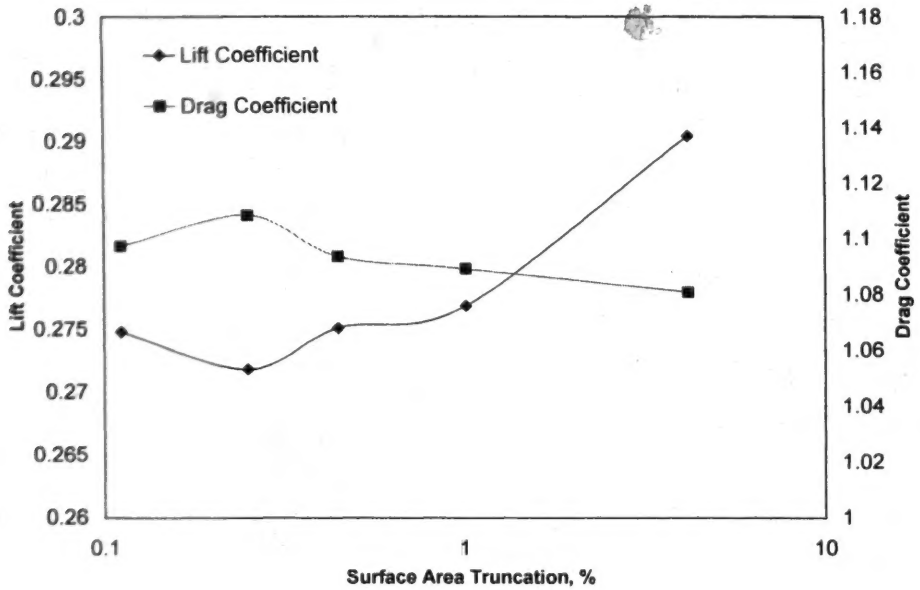

Figure 3.7 Geometric convergence results for a sphere contacting a plane at a sphere Reynolds number of 250.

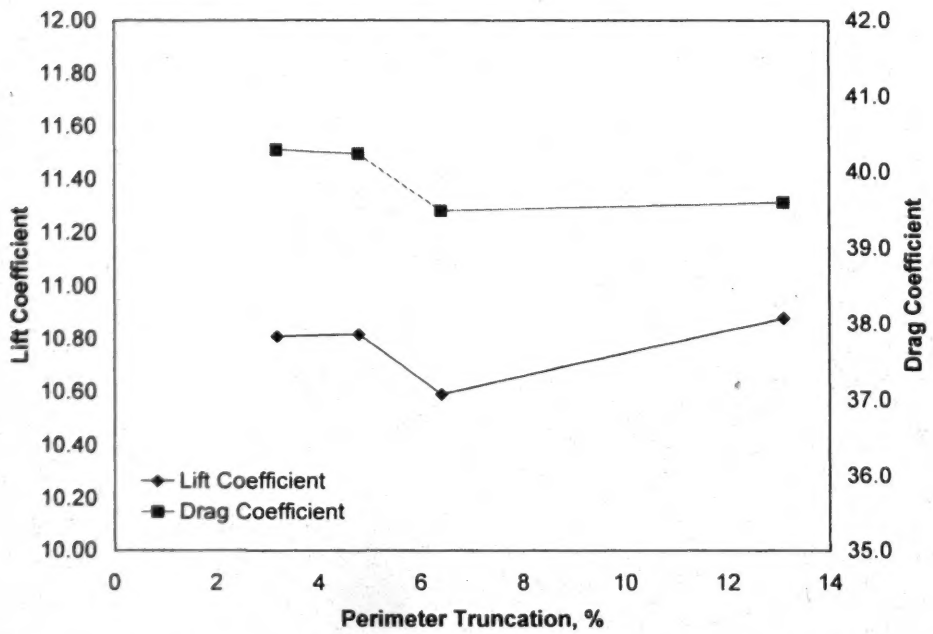

Figure 3.8 Geometric convergence results for a cylinder contacting a plane at a cylinder Reynolds number of 50.

3.5 Boundary Placement Convergence

The placement of boundaries, specifically the inlet and openings, was examined for its influence on the coefficients of force. Boundary placement convergence studies were undertaken at the Reynolds endpoints and midpoint of the studies. The placement of the top opening was examined separately from the inlet and other opening boundaries. Figures 3.9, 3.10, and 3.11 display the convergence results for the case of a sphere attached to a wall at sphere Reynolds numbers of 0.1, 10, and 250, respectively. They indicate a slightly decreasing trend of boundary placement importance with increasing Reynolds number. Consequently, the results of the Re_{sphere}= 0.1 boundary placement study were used for simulations in the range $0.1<Re_{sphere}<10$, and the Re_{sphere}= 10 study were used for simulations in the range $10<Re_{sphere}<250$.

The top far-field boundary placement influence on the solution was examined at the sphere Reynolds number of 250. At this Reynolds number, the ratio of the sphere diameter to the domain height, or blockage ratio, is highest. Consequently, the top boundary placement is expected to have the largest influence at the largest Reynolds number in the study. The height of the domain was varied from δ to 2δ, where δ was arbitrarily chosen to be $1.9\delta_{99}$, and the coefficient of lift and drag changed by 1.9% and 3.3%, respectively. This indicates that resolving δ for the remainder of the simulations will produce accurate results.

Boundary convergence studies are presented for the case of a cylinder attached to a wall in Figures 3.12, 3.13, and 3.14, for the cylinder Reynolds numbers 0.1, 10, and 49. At a cylinder Reynolds number of 49, the domain height was changed from 21 diameters to 29 diameters and a change of 0.24% and 0.23% for coefficient of drag and lift, respectively.

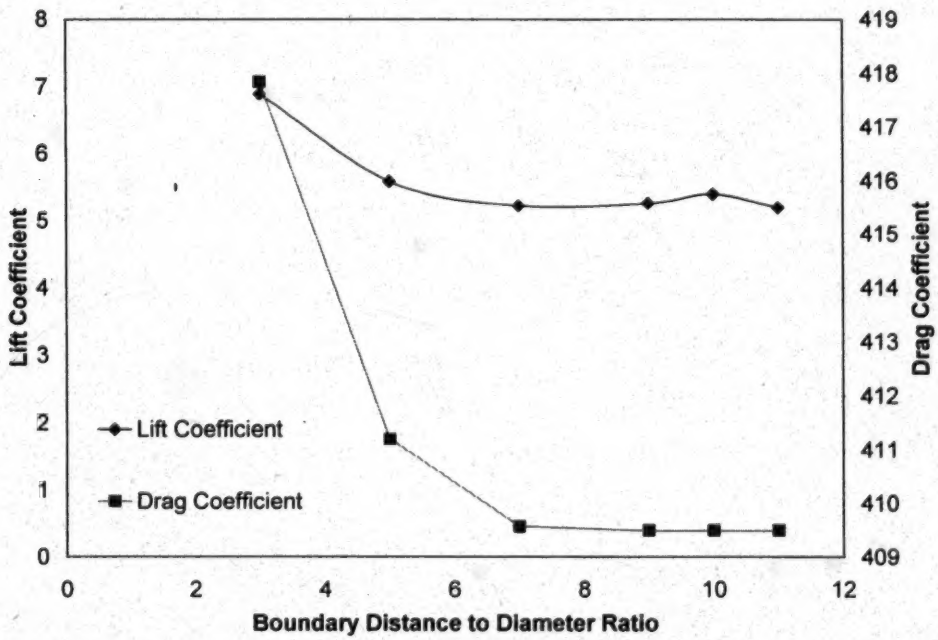

Figure 3.9 Boundary convergence study for the sphere geometry at sphere Reynolds number of 0.1. Inlet, opening (side), and opening (outflow) were moved simultaneously.

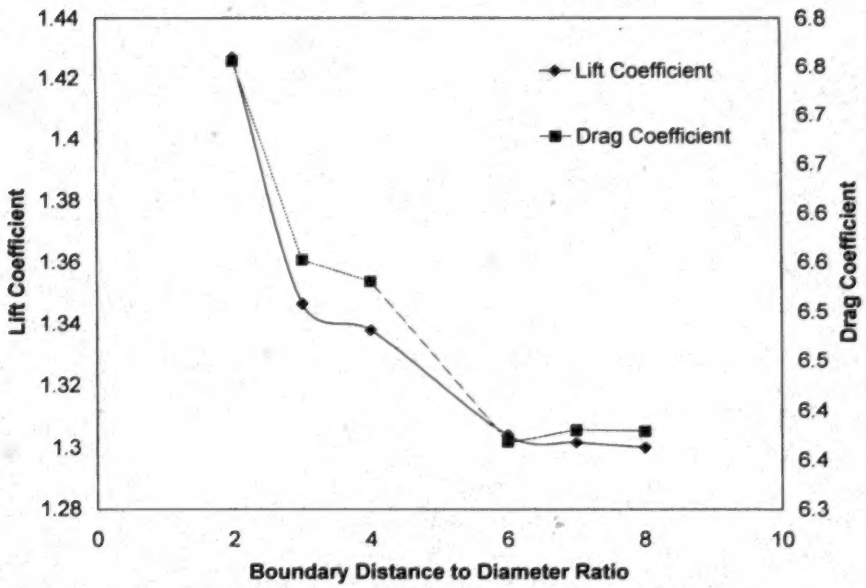

Figure 3.10 Boundary convergence study for the sphere geometry at sphere Reynolds number of 10. Inlet, opening (side), and opening (outflow) were moved simultaneously.

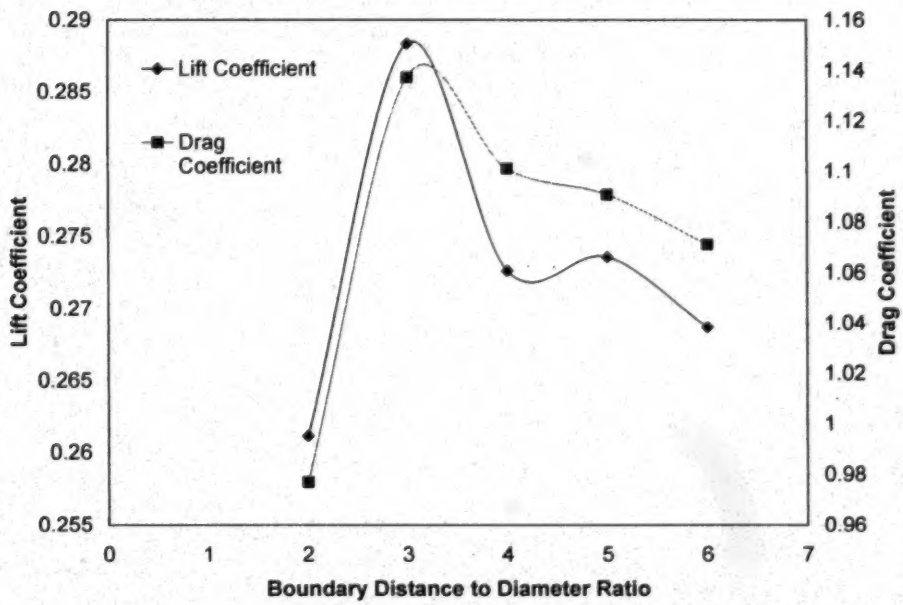

Figure 3.11 Boundary convergence study for the sphere case at a sphere Reynolds number of 250. Inlet, opening (side), and opening (outflow) were moved simultaneously.

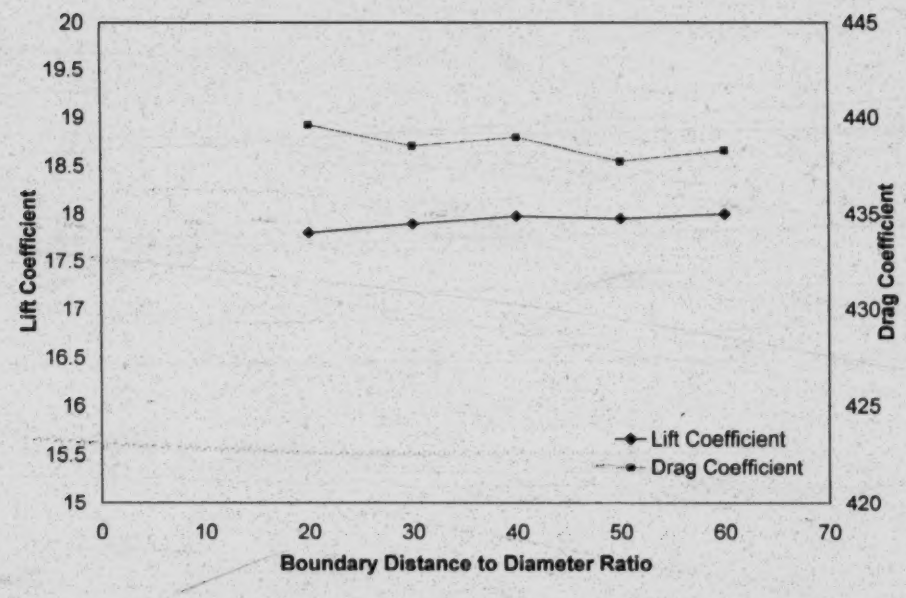

Figure 3.12 Boundary convergence study for the cylinder study at a Reynolds number of 0.1. Inlet, opening (side), and opening (outflow) were moved simultaneously.

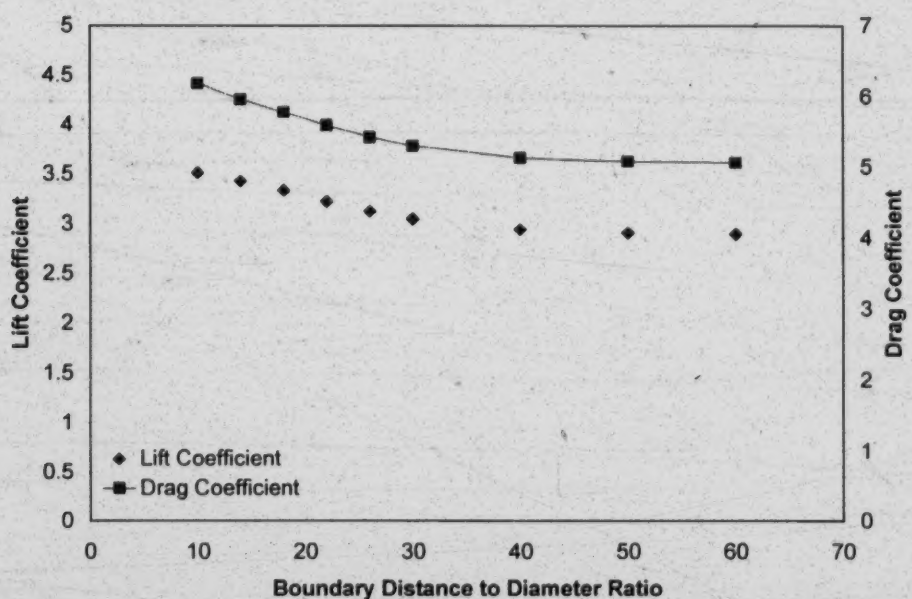

Figure 3.13 Boundary convergence study for the cylinder study at a Reynolds number of 10. Inlet, opening (side), and opening (outflow) were moved simultaneously.

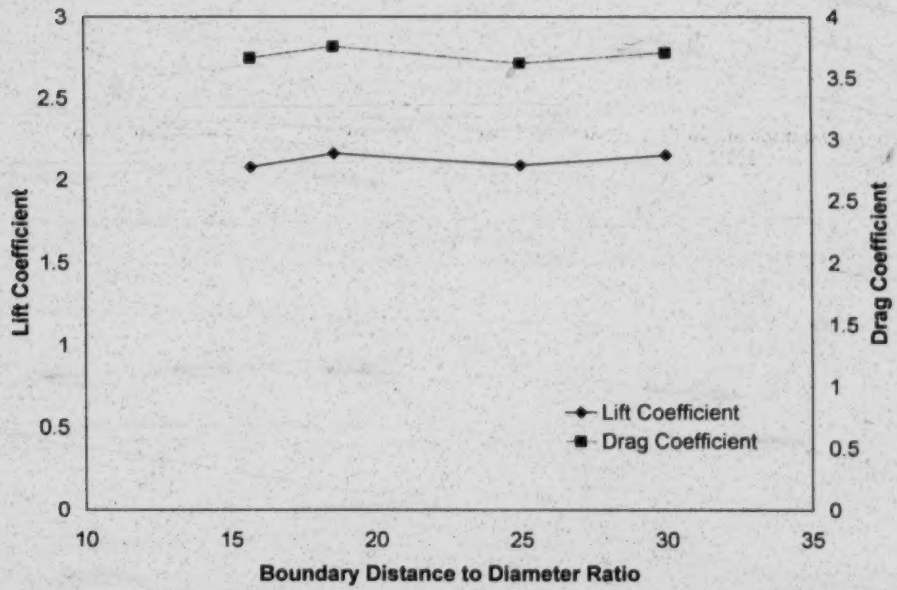

Figure 3.14 Boundary convergence study for the cylinder study at a Reynolds number of 49. Inlet, opening (side), and opening (outflow) were moved simultaneously.

3.6 Validation

There are many sources of error in a numerical solution to the Navier-Stokes equations. To further enhance the reliability of the results, a critical component of a numerical study is comparing predicted results to experimental or analytical data. In the subject under consideration, there exist analytical results for $Re_{sphere} \rightarrow 0$ and experimental results on lift at high sphere Reynolds number. The numerical results for the case of a cylinder attached to a wall in a Blasius boundary layer can not be validated due to the lack of experimental and analytical results.

At high Reynolds number, Willets and Naddeh[17] produced some experimental results. In the Reynolds range of 43 – 100, they measured a coefficient of lift of 0.4 ± 0.08. In the numerical study, the coefficient of lift varies between 0.47 – 0.67 for the Reynolds range 43 – 100, which overlaps the experimental range of values for the data point. Willets and Naddeh report two more values of lift coefficient for two more ranges of Reynolds number, as shown in Table 1. These measurements do not correlate well with the simulation predictions. The largest discrepancy is in the Reynolds number range 83 – 140 where the experimental coefficient of lift was measured to be 0.05 ± 0.02 and the corresponding numerical predictions for lift coefficient is 0.51 – 0.39.

At low sphere Reynolds number, the flow about the sphere becomes linear shear, and the analytical results for lift and drag coefficient are known. At the lowest sphere Reynolds number simulated, Re_{sphere}= 0.1, the coefficient of lift was calculated to be 5.4017, which is 7.79 % lower than the analytical result. It is clear from Figure 3.1 that the coefficient of lift is asymptotically approaching the analytical result and the difference in lift coefficient at Re_{sphere}= 0.1 is likely physical. The coefficient of drag at Re_{sphere}= 0.1 was calculated to be 409.5 in the simulation and the analytical value is 408.2, which represents a 0.3% error. In addition, the coefficient of drag values from the simulation in the range $0.1<Re_{sphere}<0.71$ were curve-fitted with a power function and the resulting formula follows.

$$C_D = 1.71 \cdot \frac{24}{\mathrm{Re}} \qquad (32)$$

The coefficient the curve-fit from Eqn (32) is 0.6% higher than the analytical value.

3.7 Curve Fitting

The results of this research were fitted into a functional form using nonlinear regression. The data was fitted using the Gauss-Newton method of optimization. The base functions were chosen as exponentials due to the wide range of Reynolds number considered as well as to force the functions to display analytical asymptotic properties at low sphere Reynolds number. The coefficient of drag was broken into two functions, the analytical function $C_{D,ana}$ (valid at low Reynolds number) and the relative difference between the analytical data and simulation results, i.e.

$$C_D = \frac{C_{D,ana}}{1 - y(\mathrm{Re}_{sphere})} \qquad (33)$$

The data for $y(\mathrm{Re}_{sphere})$, for the case of a sphere attached to a wall, is shown in Figure 3.15. The trend was fitted adequately with the following exponential.

$$y(\mathrm{Re}_{sphere}) = 0.2817\,\mathrm{Re}^{-0.0826}\, a\sinh(0.238\,\mathrm{Re}) \qquad (34)$$

The absolute relative error between the drag coefficient curve-fit and the simulation data is shown in Figure 3.16, with the maximum error being 4.3%. This error is of the same order as the simulation.

For the case of a circular cylinder attached to wall, an analytical expression for drag in creeping flow conditions does not exist. The low Reynolds number results of the simulation, in the Reynolds number range $0.06<Re<0.47$, were used to fit a function similar to $C_{D,ana}$ for the sphere. The function was generated with nonlinear regression and is as follows.

$$C_{D,ana} = 33.187/\mathrm{Re}^{0.9175} \tag{35}$$

An equation just like Eqn (33) was then used but with the cylinder replacing the sphere. The data for $y(Re_{cylinder})$, generated using Eqn. (35), for the case of a cylinder attached to a wall, is shown in Figure 3.17. The trend was fitted with the following exponential function.

$$y(\mathrm{Re}_{cylinder}) = 0.1363\,\mathrm{Re}^{-0.0993}\, a\sinh(1.0643\,\mathrm{Re}^{1.9112}) \tag{36}$$

The absolute relative error between the drag coefficient curve-fit and the simulation data, for the case of a cylinder attached to a wall, is shown in Figure 3.18, with the maximum error being 4.05%

A sum of two hyperbolic tangent functions was used to fit the lift coefficient data for the case of a sphere attached to a wall.

$$\begin{aligned} C_L &= 5.811 - 4.339\,\mathrm{Re}^{0.0429}\tanh\left(0.9395\,\mathrm{Re}^{0.3531} - 0.2966\right) \\ &+ 0.0589\tanh\left(-0.1137\,\mathrm{Re} + 2.5386\right) \end{aligned} \tag{37}$$

The absolute relative error compared to the simulation data is shown in Figure 3.16, with a maximum of 3.7%.

Both the fitted coefficient of lift and drag functions, Eqns (33) and (37), are valid for the sphere Reynolds number range $0<Re_{sphere}<250$.

The coefficient of lift for a cylinder attached to a wall was fitted with a simplified version of Eqn (37).

$$C_L = -7.5863 + 35.6496\,\mathrm{Re}^{0.008024}\tanh(0.5561\,\mathrm{Re}^{-0.185}) \qquad (38)$$

The absolute relative error compared to simulation data for is shown in Figure 3.18, with the maximum error being 1.64%. The empirical functions, Eqns (36) and (38), describing the evolution of drag and lift acting on a cylinder attached to a wall are valid in the cylinder Reynolds number range $0.06<Re_{cyinder}<49.2$.

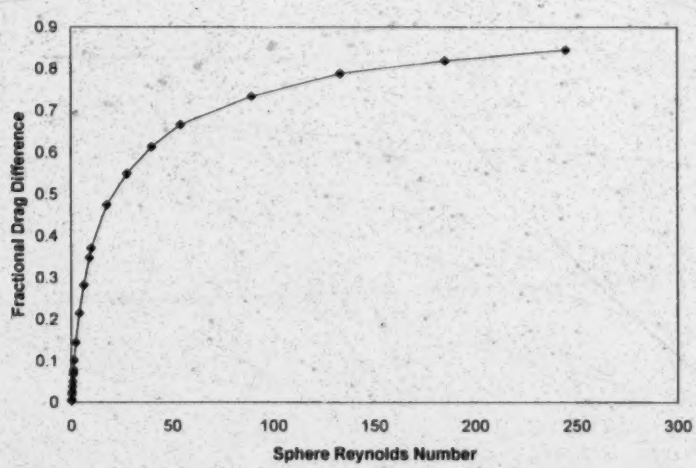

Figure 3.15 The ratio of difference between the simulated drag force (actual) and the analytical drag force to the numerical drag force for a sphere attached to a wall.

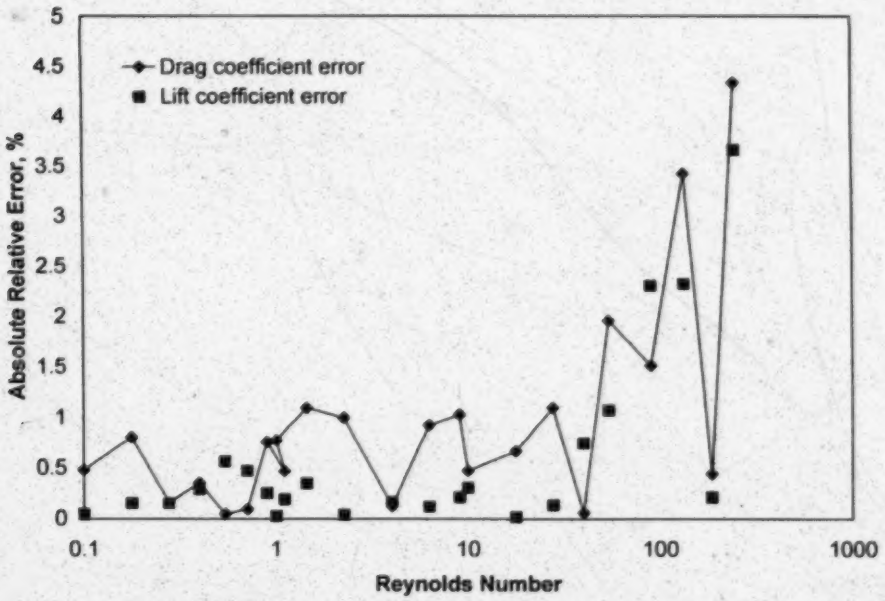

Figure 3.16 The absolute relative error between the curve-fitted functions for lift and drag and the simulated values for the case of a sphere attached to a wall.

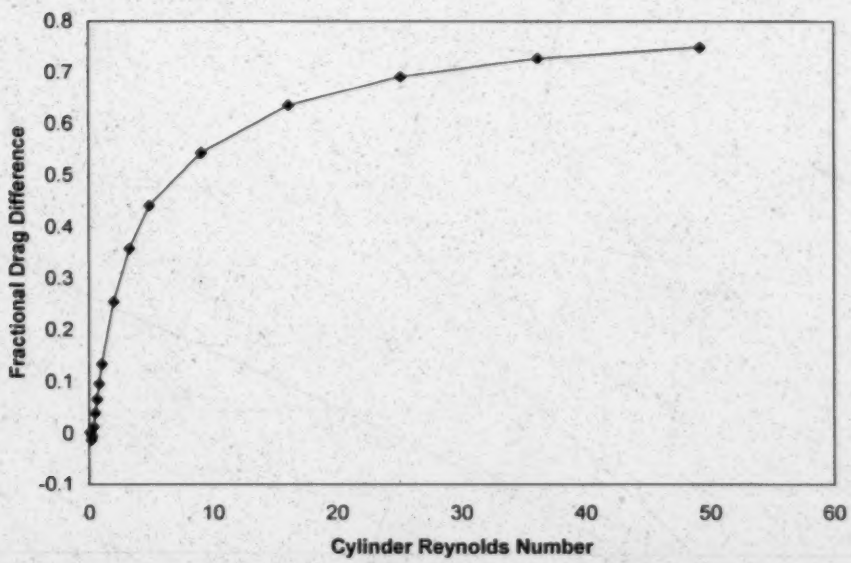

Figure 3.17 The ratio of difference between the simulated drag force (actual) and the analytical drag force to the numerical drag force for a cylinder attached to a wall.

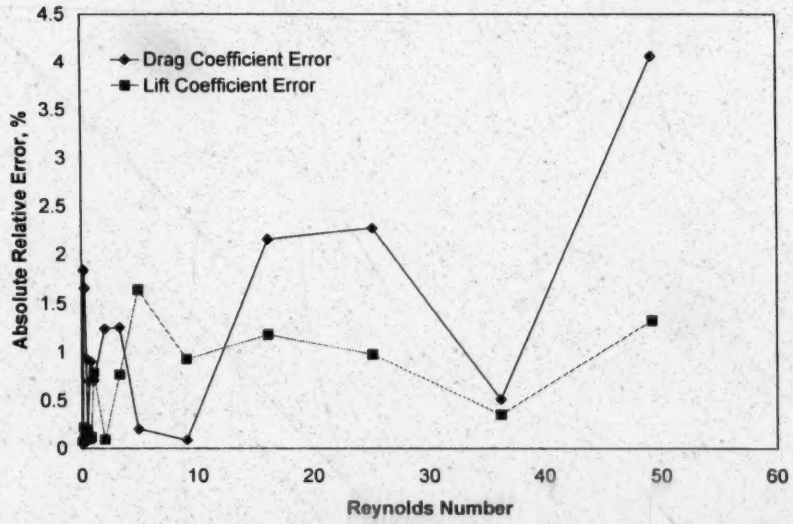

Figure 3.18 The absolute relative error between the curve-fitted functions for lift and drag and the simulated values for the case of a cylinder attached to a wall.

3.8 Flow Field Visualization

Contour plots and streamline plots are shown for the cylindrical geometry at a Reynolds number of 0.06 in Figures 3.19 and 3.20, respectively. Low Reynolds number symmetry is apparent from these plots. At a Reynolds number of 49, similar plots are presented in Figures 3.21 and 3.22. For the case of a sphere attached to a wall, contour and streamline plots are presented for Reynolds numbers of 0.1 and 250 in Figures 3.23 through 3.26.

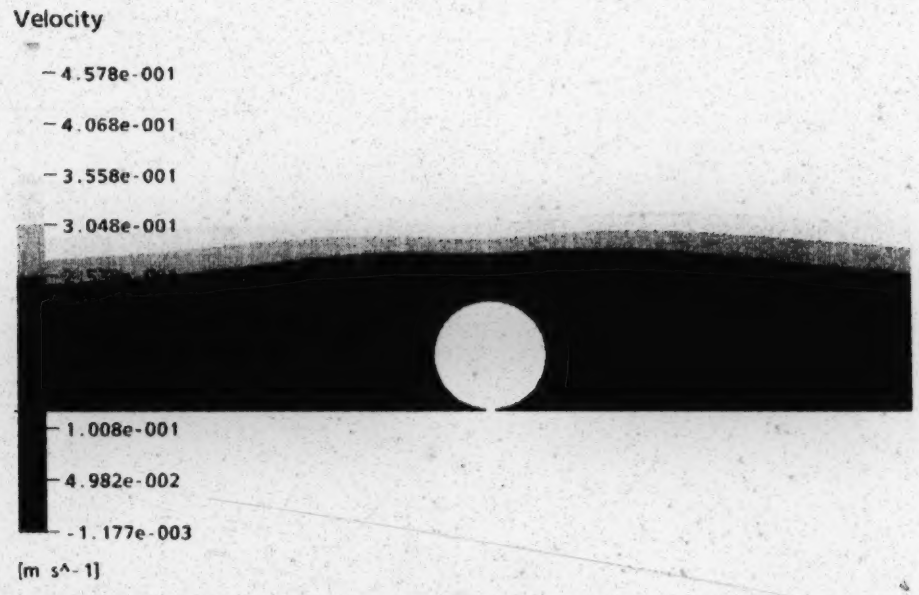

Figure 3.19 A velocity contour plot of a cylinder attached to a wall at a cylinder Reynolds number of 0.06.

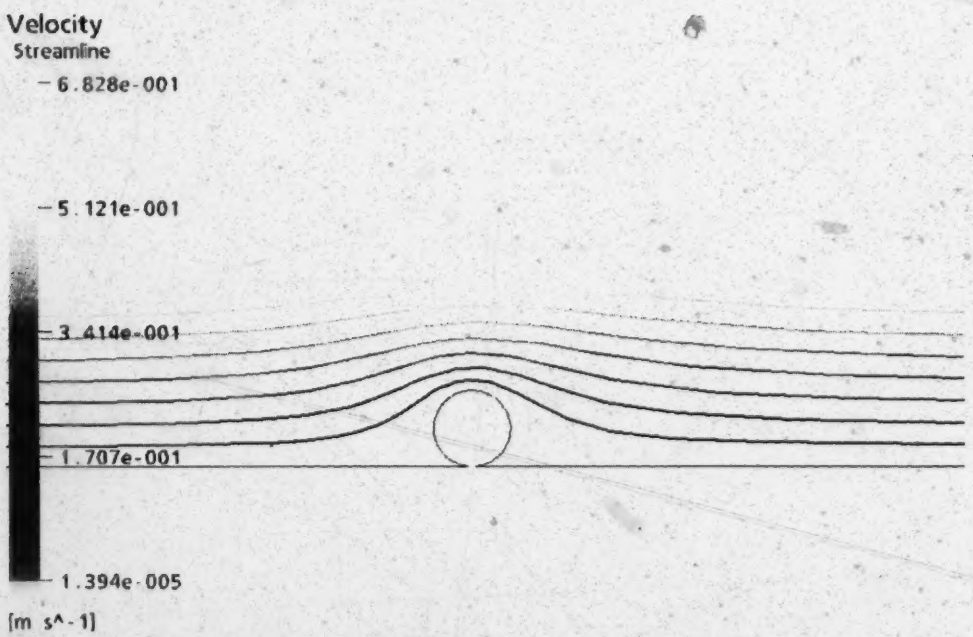

Figure 3.20 A streamline plot of a cylinder attached to a wall at a cylinder Reynolds number of 0.06.

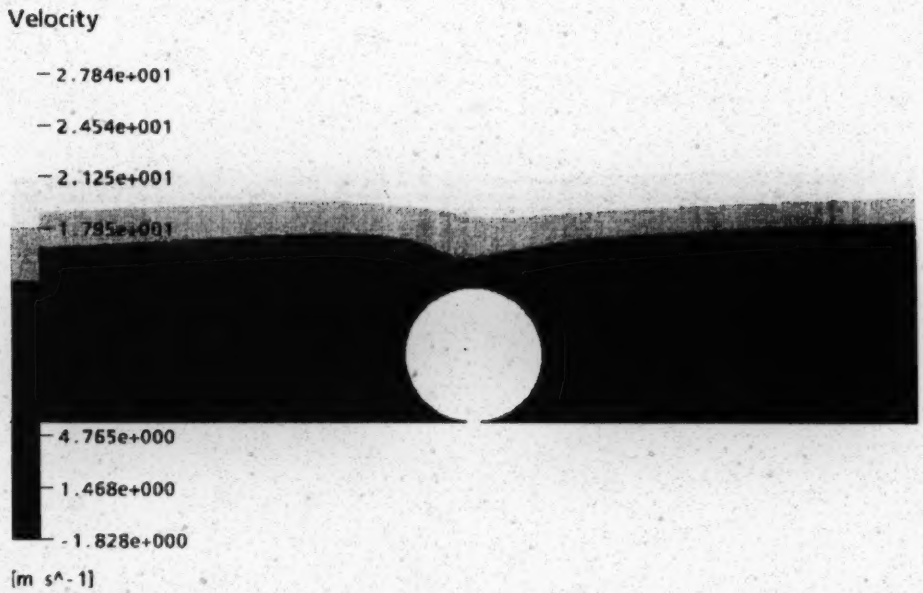

Figure 3.21 A velocity contour plot of a cylinder attached to a wall at a cylinder Reynolds number of 49.

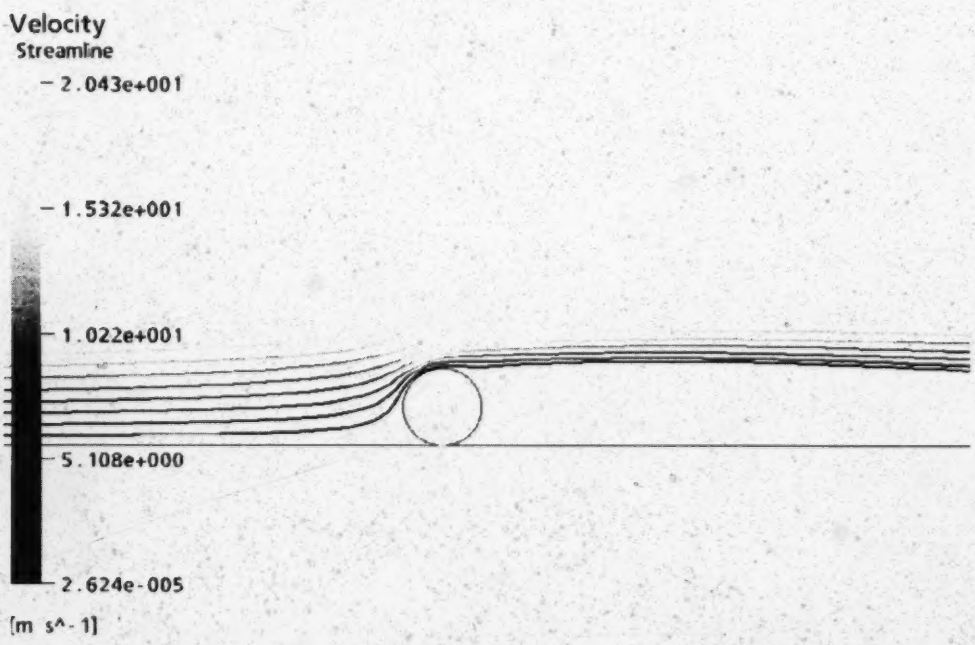

Figure 3.22 A streamline plot of a cylinder attached to a wall at a cylinder Reynolds number of 49.

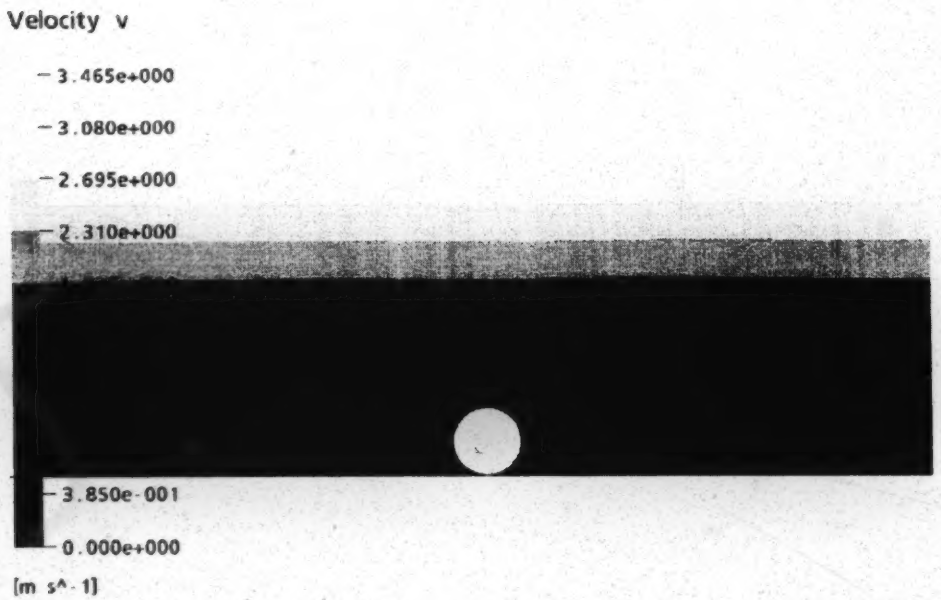

Figure 3.23 A contour plot on the streamwise symmetry plane of the sphere showing velocity variation at a Reynolds number of 0.1.

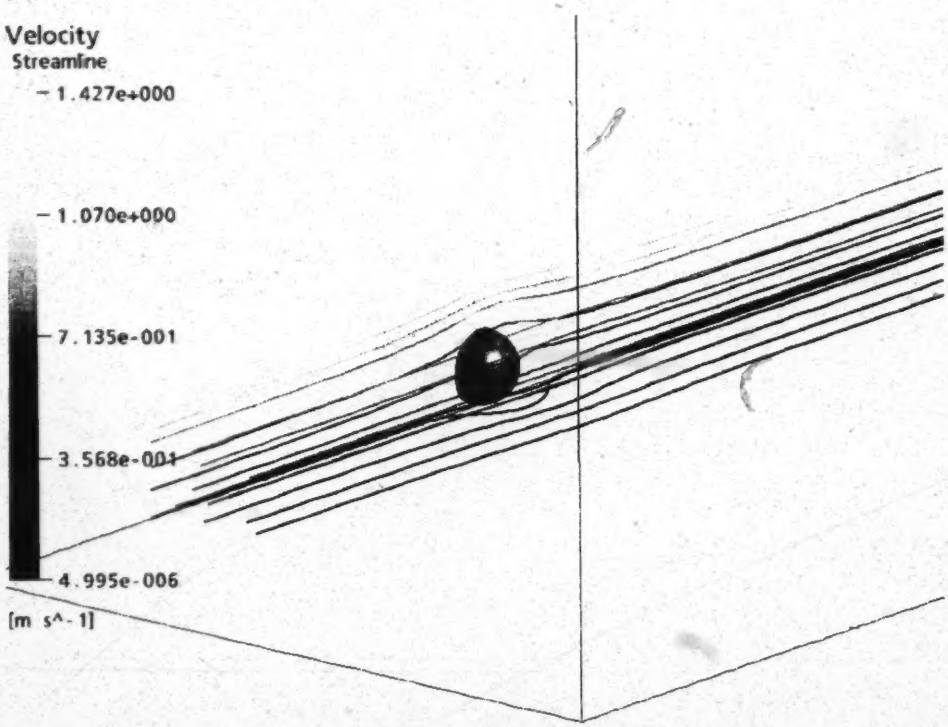

Figure 3.24 A plot on the streamwise symmetry plane of the sphere showing streamline variation at a Reynolds number of 0.1.

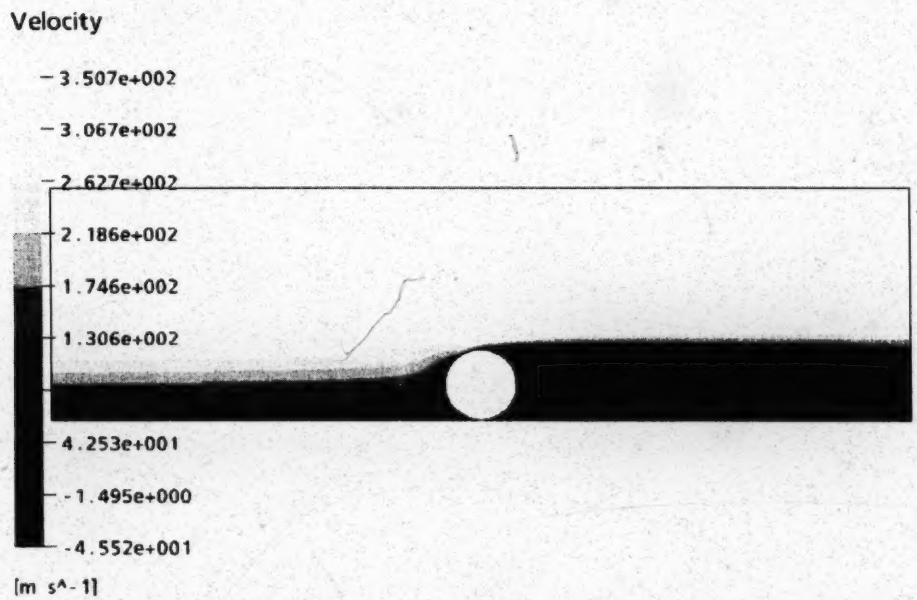

Figure 3.25 A contour plot on the streamwise symmetry plane of the sphere showing velocity variation at a Reynolds number of 250.

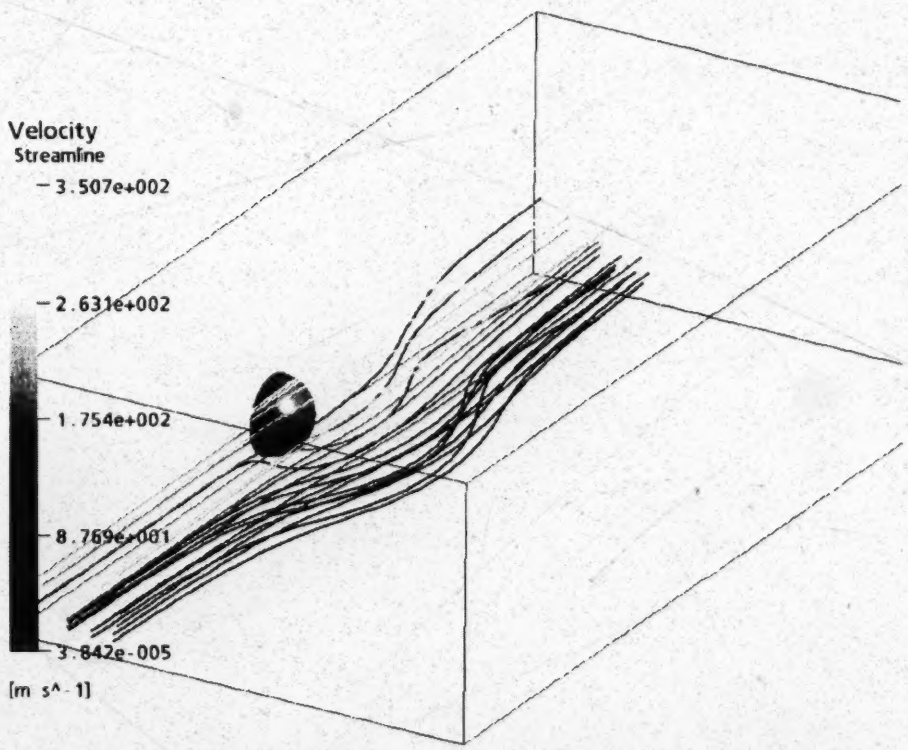

Figure 3.26 A plot on the streamwise symmetry plane of the sphere showing streamline variation at a Reynolds number of 250.

Chapter 4

Discussion

4.1 Model Accuracy

A great deal of effort was expended to ensure the simulation produced accurate results. A benefit of studying laminar flow is that no modeling approximations beyond those used to derive the Navier-Stokes equations are utilized. Thus, the mechanics equations are solved directly and precise field information does not have to be blurred through the process of time-averaging, and the additional approximate closure models do not need to be introduced. Consequently, the error in this study is due to boundary conditions, the domain, the method the equations are solved, and machine limitation. As discussed in Chapter 2, the largest sources of error are discretization error, boundary placement error, and geometric convergence error.

4.1.1 Convergence Studies

The boundary conditions used in this model, besides the inlet and no-slip wall conditions, are not exact. However, they satisfy a critical condition,

which is to allow mass and momentum transfer both into and out of the domain. Setting the first derivative with respect to boundary normal equal to zero is a widely used, inexact, and an incompletely understood boundary condition. Utilizing this boundary condition is the primary reason the placement and orientation of the boundaries have an influence on the simulated sphere lift and drag forces. However, judicious usage of the outflow boundary condition can yield accurate results, as was shown in the boundary placement studies. The boundary placement convergence studies indicated a decreasing importance of boundary placement with increasing Reynolds number. This is expected because, as Reynolds number shrinks, the influence of the sphere on the velocity and pressure field solutions grows. An analogy can be drawn against the solutions of uniform flow about a sphere with no wall present. In the creeping flow solution of uniform flow about a sphere, the stream-wise velocity is retarded 3.75% at a distance of 10 sphere diameters. The potential flow solution for uniform flow about a sphere (high Reynolds number) indicates a 6.25×10^{-3}% change in velocity at an identical number of sphere diameters. Clearly, it is expected that approximate boundary conditions must be placed further away at low Reynolds number to obtain accurate numerical calculations.

In this study, an atypical geometry convergence study was needed to ensure model accuracy. The domain itself was modified to be an approximation to the exact geometry under consideration. This was

implemented to overcome meshing difficulties encountered when considering the singular point that arises at the contact position of a sphere and plane. An alternative solution to geometric modification could be to map the domain into a different domain using a transformation. One such transformation that could be used, and was utilized in the low Reynolds number analytical shear flow solution to the problem, is the tangent-sphere transformation.

$$x = \frac{\mu \cos\psi}{\mu^2 + \nu^2}$$
$$y = \frac{\mu \sin\psi}{\mu^2 + \nu^2} \qquad (39)$$
$$z = \frac{\nu}{\mu^2 + \nu^2}$$

A sphere tangent to the x-y plane is generated by holding ν constant.

$$x^2 + y^2 + (z - 1/2\nu)^2 = 1/4\nu^2 \qquad (40)$$

This method removes the necessity of geometric approximation from the analysis, yet introduces difficulty in the numeric approximations of differential operators. This type of transformation was not possible in the commercial code used. Consequently, using a domain modification via geometric approximation was the practical solution. Two methods of geometric approximation exist. The method adopted in this study was to place a small diameter cylinder vertically from the contact point to the sphere. An alternate geometric modification would be to truncate the sphere and place it on the plane. In this method, the solution is more sensitive to geometry change

because the entire sphere is shifted vertically in the boundary layer whereas with the cylinder-truncation method only a small area near the base of the sphere is affected. However, both methods have the potential to model the idealized geometry.

The geometry convergence study showed that the lift and drag on the sphere at a Reynolds number of 250 were relatively unaffected by the truncation. At 4.17% truncation of the sphere area, the lift and drag coefficients changed by only 5.69% and 1.52%, respectively, from the surface area truncation level of 0.11%. For the case circular cylinder case, a perimeter truncation change from 13.1% to 3.19% resulted in lift and drag coefficient changes of 0.07% and 0.14%, respectively. This is important from a physical perspective because it indicates that the lift and drag coefficients have low sensitivity to the geometry of the point of contact. A real sphere or cylinder contacting a real planar surface results in a complicated geometry which depends upon the material properties of the sphere and the wall as well as the various forces acting on the bodies. The convergence study indicates that the lift and drag coefficient results are applicable to moderately deformable spheres and cylinders without a great loss in accuracy.

The geometric convergence results are more important at a high Reynolds number than at low. This result can be inferred from analytical solutions involving a sphere and a disk in creeping, uniform flow. A sphere in creeping, uniform flow has the following formula for drag coefficient.

$$F_D = 6\pi\mu Ua \tag{41}$$

While a disk with a surface normal parallel to the flow has the following drag formula.

$$F_D = 16\mu Ua \tag{42}$$

A disk with a surface normal perpendicular to the flow has the following drag formula.

$$F_D = {}^{32}/_{3}\,\mu Ua \tag{43}$$

In the above formulas a is the disk radius. The difference between the disk formulas and the sphere formula for drag force, as pointed out by White[29], is only 15% and 43% for the disk surface vector parallel and perpendicular to the flow, respectively. Despite the tremendous difference in geometry and orientation, the drag forces remain similar. Hence, the geometry convergence would be expected to have a less pronounced effect at low Reynolds number than at high.

The largest source of error in the simulation of a sphere attached to a wall was discretization error. Due to restrictions on computational capacity, grid convergence was deemed complete when the lift or drag coefficient changed less than 3%. This error could be reduced with increased computational capacity. The detailed grid convergence test showed monotonic convergence of lift and drag coefficient on the three most refined meshes, which according to Ferziger and Peric[32] is a necessary result for obtaining grid

convergence on unstructured meshes. This contrasts the case of a cylinder attached to a wall, where sufficiently fine grids were used to drive changes in coefficient of lift and drag under 0.25%.

Another source of error arises from the iterative solution of the set of nonlinear algebraic equations. The maximum mass and momentum residuals of the solution were driven to a steady value of $\sim 10^{-7}$ in the solution of all models. The residual level could be reduced by orders of magnitude if double precision were used. The effect of double precision solution on the sphere simulation was checked on a coarse and refined grid. Double precision was found to have negligible influence on lift and drag coefficient when the grid size was greater than 400 000 nodes. At a sphere Reynolds number of 1, a grid with 23 826 nodes showed a change of 0.78% and 3.22% for coefficient of drag and lift, respectively, when solved with double precision. With a grid of 102 736 nodes, the coefficient of drag and lift changed by 0.28% and 2.09%, respectively. When refinement was changed to 400 000 nodes, the changes in both coefficients were less than 0.5%. In the cylinder simulations, the residuals were driven to a value of 10^{-6}. Upon comparison to identical simulations driven to a residual of 10^{-8}, the coefficients of lift and drag changed less than 0.98% and 0.14%, respectively, indicating algebraic convergence.

4.1.2 Validation

Validation in this study solely considers the case of a sphere attached to a wall due to the lack of analytical or experimental results for a cylinder. At high sphere Reynolds number, the simulation predicts a lift coefficient that matches within experimental error one measurement of three provided by Willetts and Naddeh.[17] Such disagreement between experiment and simulation should not detract from the perceived accuracy of the computational results. Due to the low magnitude of the forces involved, the experiment is difficult. Actual force measurements are not stated in the results of Willets and Naddeh[17], but instead state dimensionless results without any indication of error, except perhaps the awkward reporting of Reynolds number range for which the force is valid. They used a force measuring device (capacitance changing with deflection) that was gravimetrically calibrated and had a force resolution of 0.2 mN. They utilized mineral oil (SG 0.931) in a rectangular duct and report boundary layer velocity measurements. At a sphere Reynolds number of 200, the numerical results of this study predict a coefficient of lift of ~ 0.3. At the sphere midpoint, 10 mm, they measured a velocity of ~ 0.5 m/s. From this data the lift force is calculated to be 11.8 mN. If the accuracy of the force measuring device is taken to be its resolution, a liberal approach, the measurement error is ~ 2%. If the experimental lift coefficient is used in the error analysis, the error increases to 6%, and becomes 29% for the

measurement range $83<Re_{sphere}<140$. The difficulty of the experiment was also reiterated by Muthanna et al. who adopted techniques from atomic force microscopy for measurement of lift and drag on a sphere in a low Reynolds number shear flow study.[18] The experimental apparatus is promising, yet difficulties arise in instrument calibration and sensitivity. In addition to the measurement difficulties, the experiment does not predict the monotonic trend of coefficient of lift variation with increasing Reynolds number. Certainly, small increases in Reynolds number are not expected to produce nearly an order of magnitude leap in coefficient of lift. Further experimental work needs to be completed to validate the results presented in this work.

At low sphere Reynolds number, the validation results strongly support the accuracy of the simulation. The coefficient of lift is asymptotically approaching the analytical value, as shown in Figure 3.1. At the lowest sphere Reynolds number considered in the study, the analytical value differs by 7.79% from the simulation value. However, this difference can be partially attributed to various sources of error within the simulation, such as discretization error, but is most likely a physical difference. At lower sphere Reynolds numbers, it is expected that the coefficient of lift would match the analytical result. When considering the coefficient of drag, the simulation at low sphere Reynolds number matches the analytical value to a high degree of accuracy. At $Re_{sphere}=0.11$, the analytical and simulation values match within 0.3%. These results lend a great deal of confidence in the simulation results.

The overall accuracy, or order, of the study can not be stated definitively due to the nature of unstructured grid simulations (i.e. Richardson extrapolation can not be used). However, a crude estimation of error can be generated by considering the errors in the convergence testing. The maximum grid convergence error accepted was 3% on a grid with 30% – 40% fewer nodes. The error arising from boundary placement is ~ 2%, and is ~ 2% from sphere truncation. A conservative estimation of error is created by assuming the errors are dependent and additive, which leads to a general simulation error of ± 7%

4.2 Model Results

The simulation results for a spherical body attached to a planar wall, along with empirical relationships and low Reynolds number analytical behavior are shown in Figures 4.1 and 4.2. The hydrodynamic results for a circular cylinder attached to a wall are displayed in Figures 4.3 and 4.4. The curve fitted functions relating hydrodynamic force to sphere Reynolds number, Eqns (34) and (37), are valid through the range $0<Re_{sphere}<250$. Above $Re_{sphere}=250$, the coefficients of lift and drag are expected to have a mean component in addition to a fluctuating component due to the shedding of hairpin vorticies.[19] The relationships developed for the lift and drag on a cylinder, Eqns (36) and (38), are valid in the range $0.06<Re< 49$.

The lift and drag trends, for the sphere and cylinder results, are similar over the Reynolds range examined. The defining difference between the two occurs at low Reynolds number where drag asymptotes to an infinite value and the lift asymptotes to a constant value. An important result of this work in addition to determining the lift and drag characteristics of a sphere attached to a wall in a Blasius boundary layer is determining the sphere Reynolds number at which the low Reynolds analytical results become inaccurate. Simulation data for coefficient of drag deviates by 10% from the analytical result a sphere Reynolds number of 1.6, and for coefficient of lift the analytical relationship deviates by less than 10% at a sphere Reynolds number of 0.11.

It is known that the coefficients of lift and drag presented in this work are functions of some measure of boundary layer thickness, such as the ratio of boundary layer thickness to sphere or cylinder diameter or the Reynolds number based on plate length and the particle Reynolds number. The empirical equations presented were generated at a Reynolds number with respect to plate length of 32 400. However, at close vertical distances to the wall, the Blasius boundary layer becomes a shear flow. Under the conditions of shear flow, the Reynolds particle number and the Reynolds number with respect to plate length are dependent and the force coefficients become single variable functions. Consequently, at low particle Reynolds number, the empirical functions become accurate for Blasius boundary layers at all Reynolds number with respect to plate length. As the particle Reynolds

number increases, the particle occupies a larger portion of the boundary layer and the functions developed in this study become less accurate and more dependent on the Reynolds number with respect to plate length. Considering the highest cylinder and sphere Reynolds numbers in this study, the particle Reynolds number which is most influenced by plate Reynolds number, boundary layer velocity profiles can be generated to show the influence of increasing plate Reynolds number. Figures 4.5 and 4.6 display various velocity profiles for a constant cylinder Reynolds number of 49 and for a constant sphere Reynolds number of 250. It is clear that as particle Reynolds number is decreased from the maximum values considered in this study that the various velocity profiles collapse into a shear profile. Since the velocity profiles differ very little at the maximum particle Reynolds number considered, especially for the cylindrical geometry, the empirical functions generated for both lift and drag coefficient can be used to predict lift and drag at plate Reynolds number other than 32 400. The accuracy of the prediction increases as the particle Reynolds number is decreased.

Should an experimentalist be interested in verifying the results presented in this study, insight into the experimental design can be gained through the empirical relationships developed in this study. The selection materials and geometry such that the forces on the sphere are maximized for a given experimental rig could be calculated, and would allow an accuracy prediction of the given force measurement system.

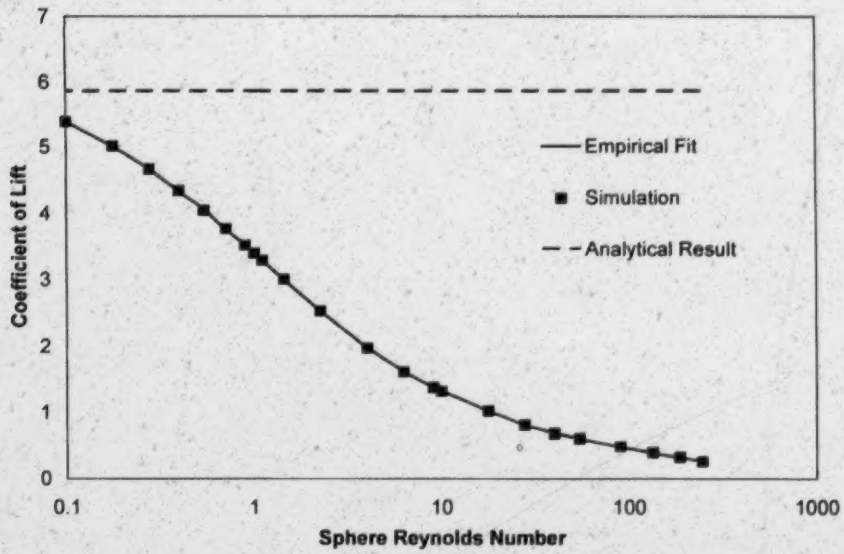

Figure 4.1 The variation of coefficient of lift for a sphere attached to a wall in a Blasius boundary layer in the Reynolds number range 0.1 – 250. Simulation and analytical results are shown as well as the empirical fit.

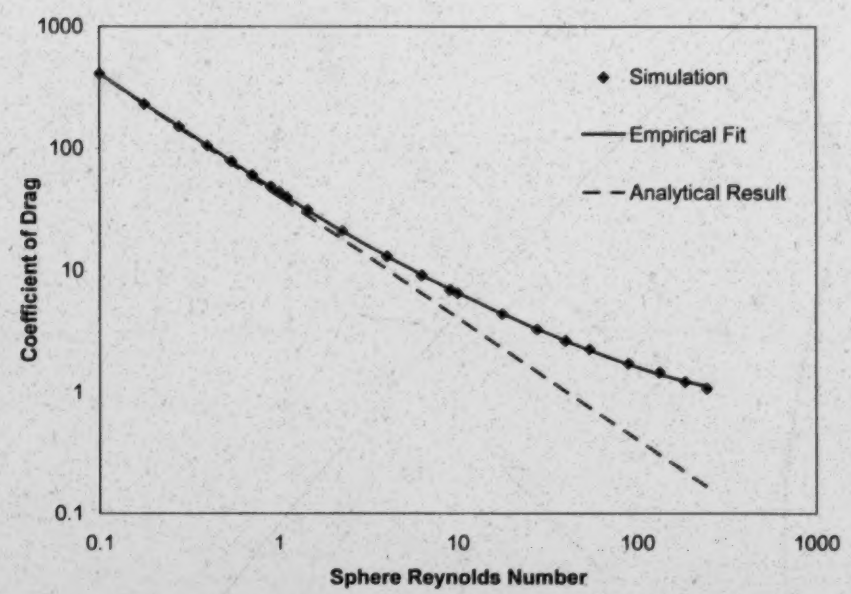

Figure 4.2 The variation of coefficient of drag on a sphere attached to a wall in a Blasius boundary layer for the Reynolds number range 0.1 – 250. Simulation and analytical results are shown as well as the empirical fit.

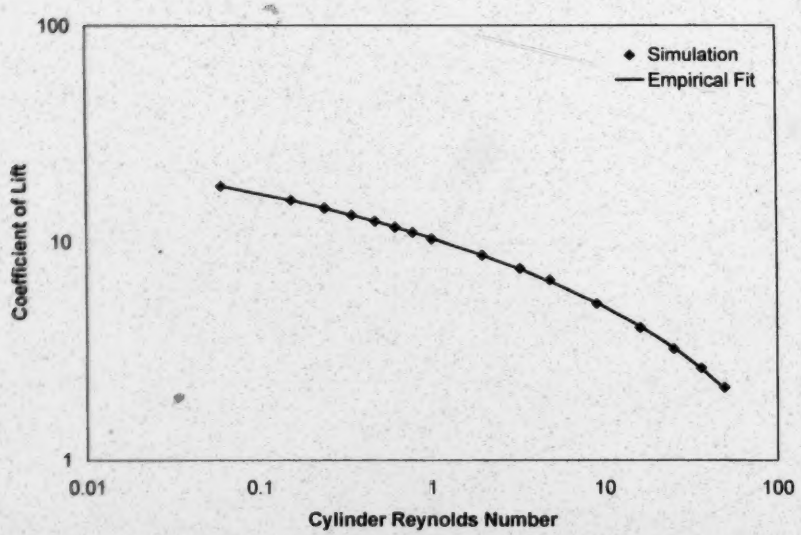

Figure 4.3 The variation of coefficient of lift for a circular cylinder attached to a wall in a Blasius boundary layer in the Reynolds number range 0.06 – 49. Simulation results are shown as well as the empirical fit.

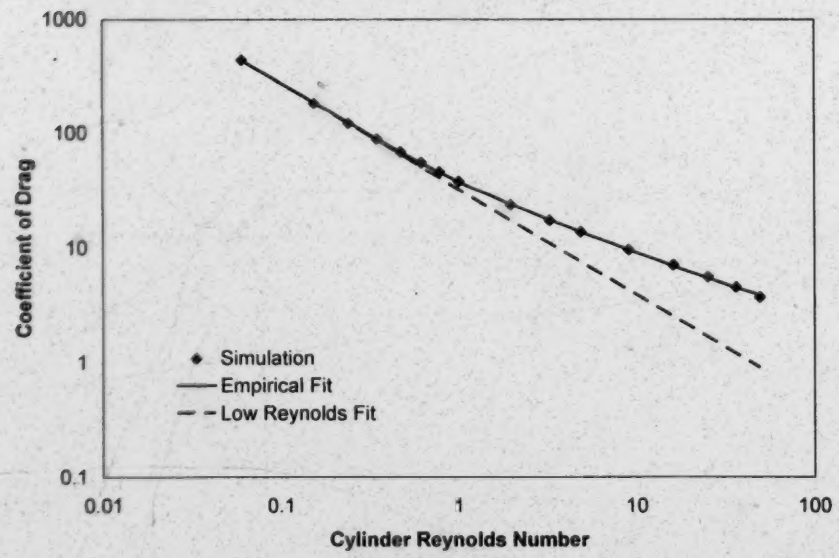

Figure 4.4 The variation of coefficient of drag for a sphere attached to a wall in a Blasius boundary layer in the Reynolds number range 0.06 – 49. Simulation results are shown as well as the empirical fit.

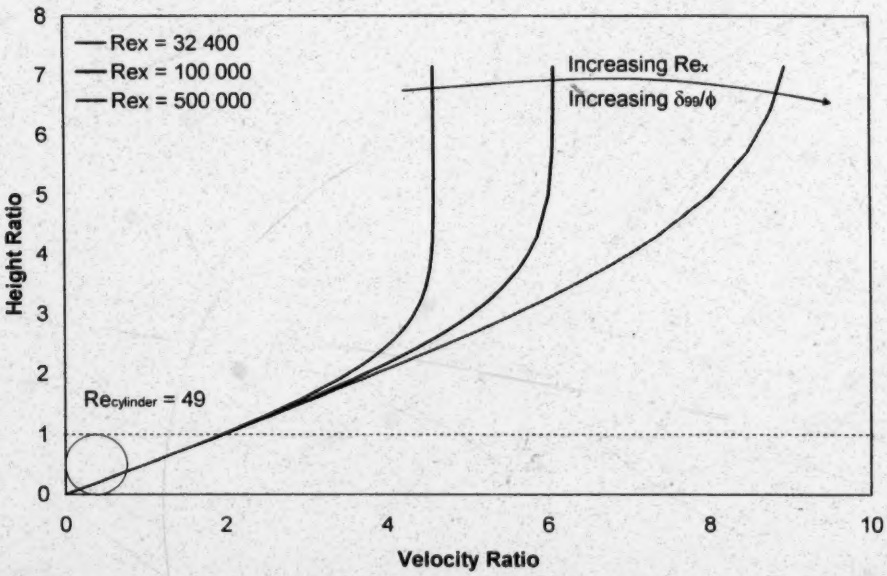

Figure 4.5 Velocity profile variation holding $Re_{cylinder}$ constant at 49. The height is normalized against cylinder diameter and the velocity against the velocity at the midpoint of the cylinder.

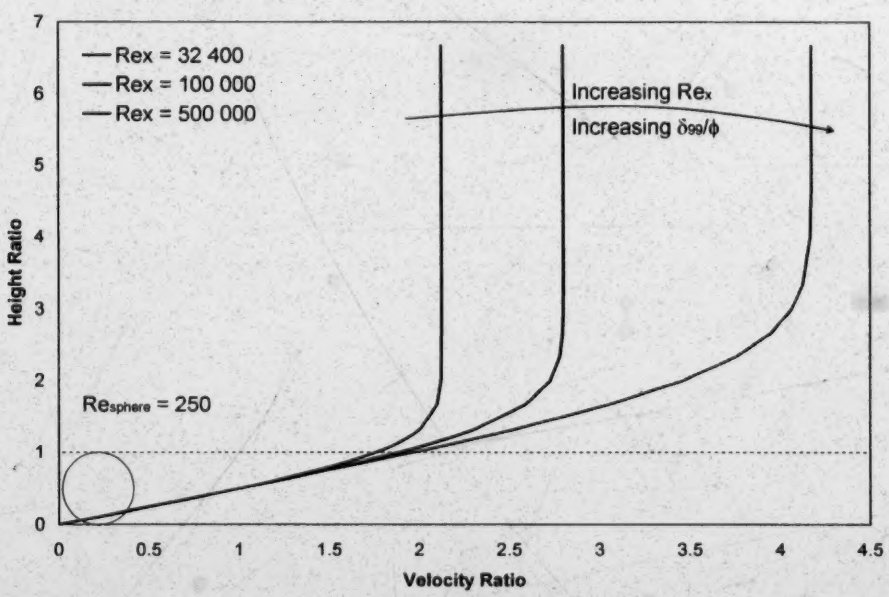

Figure 4.6 Velocity profile variation holding Re_{sphere} constant at 250. The height is normalized against sphere diameter and the velocity against the velocity at the midpoint of the sphere.

4.3 Physical Applicability

The relationships generated in this work are primarily useful for predicting impending motion of a sphere or cylinder attached to a wall in a Blasius boundary layer. Examples of such a scenario include drug particles in a dry powder inhaler in the pharmaceutical industry, removal of dust particles in a ventilation system, and incipient pollen motion. The models allow the prediction of particle movement for a boundary layer flow, or conversely the calculation of flow conditions necessary to cause particulate impending motion. Incipient motion models are typically created through the consideration of moment and force balances on a characteristic particle, or atypically by considering the energy of the system. For both sets of models to be successful, the forces acting on the sphere must be well-characterized. Knowledge of the hydrodynamic forces is but one aspect of the solution. A notable obstacle in such a model is the characterization of the electrostatic interaction between the wall and the particle. Electrostatic interactions are known to be highly dependent upon the geometry near the point of contact. Consequently, highly detailed geometric information must be known to accurately predict electrostatic forces. It is clear from this discussion that statistical analysis lends itself to resuspension or impending motion models. In realistic situations, particles with a range of sizes lie on a flat plate with a given roughness. This scenario gives rise to a distribution of lift and drag forces, for

which there is a corresponding distribution of electrostatic forces, gravitational forces, and geometric information. The model will not be developed in this work, as that is not the objective, but this work has direct consequences in such analysis.

4.4 Extension of Work

A simple extension of this work would be to characterize the unsteady lift and drag forces on a circular cylinder or sphere attached to a plate in a Blasius boundary layer prior to turbulent transition. Further, experimental evidence could be generated to either support or modify the results presented in this work. Analytical results for creeping shear flow past a cylinder attached to a wall could be generated to extend the low Reynolds number validity of the lift and drag functions.

In physical situations, rarely does a single, approximately spherical or cylindrical object stand alone on a plate. There are often many objects, and such is the case with dry powder inhalers in the pharmaceutical industry. It would be practical to examine the variation in lift and drag coefficients of a sphere or cylinder attached to a wall due to the varying proximity of other particles. Also, realistic particles often have rough surfaces and an investigation of the influence of average asperity size on the lift and drag trends as well as the Reynolds number at which the flow regime becomes unsteady would be interesting.

Possibly the most important extension of this work is to determine how sensitive the empirical relationships developed in this study are to the Reynolds number with respect to plate length.

Chapter 5

Summary

Determining the forces on a solid body is a fundamental and important task in fluid mechanics. It is a difficult undertaking that most often does not yield to existing analytical methods, which makes computational or experimental characterization necessary. An object and flow condition that lends itself to computational analysis is laminar flow about a sphere, or a circular cylinder in the two-dimensional case, attached to a planar wall in a Blasius boundary layer. This model represents an approximation to many physical situations, including flow in a dry powder inhaler, flow over substrates containing contaminants in microelectronics fabrication, and atmospheric flows over roughly planar surfaces holding roughly spherical particles (pollen, sand, etc.). The aim of this research was to characterize the lift and drag forces on a sphere and a circular cylinder attached to a wall in a Blasius boundary layer under the constraint of laminar, steady flow about the

sphere. Additionally, the Reynolds number with respect to plate length was held constant at 32 400.

A commercially available computational fluid dynamics software package was used to model the two geometries over a sphere Reynolds number range of 0.1 – 250 and a cylinder Reynolds number range of 0.06 – 49. Detailed convergence testing was completed to ensure model accuracy, including grid convergence and boundary placement testing. The computational domain utilized a modified geometry, where the contact point singularity of the sphere was removed through the placement of a vertical cylinder intersecting the wall and the sphere. For a cylinder placed tangent to a planar surface, the singular line was removed through the placement of a rectangular box at the point of intersection. Convergence testing was also completed on the geometry to determine the influence of geometric modification on coefficient of lift and drag. The sphere simulation was validated at low Reynolds number with analytical solutions and at high Reynolds number with experimental data for coefficient of lift. The problem consisting of a circular cylinder placed tangent to a wall and normal to the freestream direction has yet to be examined, either experimentally or analytically, in the scientific community. Thus, the cylindrical results generated in this study were not validated.

The convergence results indicated that accurate results could be obtained if the top boundary was placed such that the boundary layer, δ, was

completely resolved. Additionally, the influence of the remaining boundaries was studied simultaneously at the sphere Reynolds numbers 0.1, 10, and 250, and at cylinder Reynolds numbers of 0.06, 10, and 49. The results indicated that convergence was obtained at distance to sphere diameter ratios of 7, 6, and 6, respectively, and at distance to cylinder diameter ratios of 60, 50, and 30. The geometry convergence study indicated a relative insensitivity of the force coefficients to the amount of sphere truncated. At 0.25 % truncation of sphere surface area, the lift and drag coefficients were 1.08% and 1.00% different from the 0.11% truncation. The cylinder perimeter truncation displayed a 0.14% and 0.07% change in coefficient of drag and lift when the surface area truncation was reduced from 4.8% to 3.2%. Validation results at high sphere Reynolds number for the coefficient of lift match within experimental error one of three data points generated by Willets and Naddeh.[17] At low sphere Reynolds number, the coefficient of lift is 7.79% different from the analytical result, but this is likely a physical difference, and as sphere Reynolds number decreases the analytical and computational results are expected to match. The coefficient of drag calculated by the simulation at $Re_{sphere} = 0.1$ was 0.3 % different from the analytical result. The results of the convergence studies were used to produce 23 data points in the sphere Reynolds range 0.1 – 250 and 16 results in the cylinder Reynolds number range 0.06 - 49. The resulting data points were curve-fitted with exponential functions which were forced to

match the low Reynolds number analytical solutions for the case of a sphere attached to a wall.

The results of the sphere simulations show the particle Reynolds number at which the analytical results deviate appreciably (10%) from the physical, thus giving limits on usage of the low Reynolds number analytical relationships. For a coefficient of drag, the analytical results should be used below a sphere Reynolds number of 1.6 and for the coefficient of lift the analytical expression is accurate up to a Reynolds number of 0.11. The physical applicability of these results lies in the domain of impending motion prediction of spherical or cylindrical particles in a Blasius boundary layer. Knowledge of the forces acting on the particle, including gravimetric, electrostatic, contact, and hydrodynamic, along with detailed geometric information at the point where the particle contacts the wall, allows calculation of the conditions necessary for rolling, sliding or vertical motion of the sphere. This research contributes understanding and insight into the hydrodynamic forces acting on the sphere and the cylinder.

Bibliography

[1] F. M. White. *Fluid Mechanics. McGraw-Hill*, New York, 1974.

[2] H. Sakamoto, and H. Haniu. The formation mechanism and shedding frequency of vortices from a sphere in uniform shear flow. *Journal of Fluid Mechanics*, 287: 151 – 171, 1995.

[3] E. Achenbach. Vortex shedding from spheres. *Journal of Fluid Mechanics*, 62(2): 209 – 221, 1974.

[4] G. Ziskind, M. Fichman, and C. Gutfinger. Resuspension of particulates from surfaces to turbulent flows – review and analysis. *Journal of Aerosol Science*, 26(4): 613 – 644, 1995.

[5] T. Loiseleux, P. Gondret, M. Rabaud, and D. Doppler. Onset of erosion and avalanche for an inclined granular bed sheared by a continuous flow. *Physics of Fluids*, 17: 103304, 2005.

[6] K. Xu, R. Vos, G. Vereecke, G. Doumen, W. Fyen, P.W. Mertens, M.M. Heyns, C. Vinckier, J. Fransaer, F. Kovacs. Fundamental study of the removal mechanisms of nano-sized particles using brush scrubber cleaning. *Journal of Vacuum Science and Technology B – Microelectronics and Nanometer Structures*, 23(5): 2160 – 2175, 2005.

[7] L. Cheng, and L. W. Chew. Modelling of flow around a near-bed pipeline with a spoiler. *Ocean Engineering*, 30(19): 1595 – 1611, 2003.

[8] H. K. Chan. Dry powder aerosol delivery systems: current and future research directions. *Journal of Aerosol Medicine*, 19(1): 21 – 27, 2006.

[9] G. K. Crompton. Dry powder inhalers: advantages and limitations. *Journal of Aerosol Medicine*, 4(3): 151 – 156, 1991.

[10] V. Berard, E. Lesniewska, C. Andres, D. Pertuy., C. Laroche, and Y. Pourcelot. Dry powder inhaler: influence of humidity on topology and adhesion studied by AFM. *International Journal of Pharmaceutics*, 232: 213 – 224, 2002.

[11] M. W. Reeks, and D. Hall. Kinetic models for particle resuspension in turbulent flows: theory and measurement. *Journal of Aerosol Science*, 32: 1 – 31, 2001.

[12] G. Ziskind, M. Fichman, and C. Gutfinger. Resuspension of particulates from surfaces to turbulent flows – review and analysis. *Journal of Aerosol Science*, 26(4): 613 – 644, 1995.

[13] P. G. Saffman. Lift on a small sphere in slow shear flow. *Journal of Fluid Mechanics*, 18(3): 385 – 400, 1965.

[14] P. Cherukat and J. B. McLaughlin. Inertial lift on a rigid sphere in a linear shear flow field near a flat wall. *Journal of Fluid Mechanics*, 263: 1 – 18, 1994.

[15] M. E. O'Neill. A sphere in contact with a plane wall in a slow linear shear flow. *Chemical Engineering Science*, 23: 1293 – 1298, 1968.

[16] D. Leighton and A. Acrivos. The lift on a small sphere touching a plane in the presence of a simple shear flow. *Journal of Applied Mathematics and Physics*, 36: 174 – 178, 1985.

[17] B. B. Willets and K. F. Naddeh. Measurements of lift on spheres fixed in low Reynolds number flows. *Journal of Hydraulic Research*, 24(5): 425 – 435, 1987.

[18] C. Muthanna, F. T. M. Nieuwstadt, and J. C. R. Hunt. Measurement of the aerodynamic forces on a small particle attached to a wall. *Experiments in Fluids*, 39: 455 – 463, 2005.

[19] M. Mochizuki. Smoke observation on boundary layer transition caused by a spherical roughness element. *Journal of the Physical Society of Japan*, 16(5): 995 – 1008, 1961.

[20] M. Mochizuiki. Hot-Wire Investigations of smoke patterns caused by a spherical roughness element. *Natural Science Report, Ochanomizu University*, 12(2): 87 – 101, 1961.

[21] S.J. Price, D. Sumner, J. G. Smith, K. Leong, and M. P. Paidoussis. Flow visualization around a circular cylinder near to a plane wall. *Journal of Fluids and Structures*, 16(2): 175 – 191, 2002.

[22] P.W. Bearman and M.M. Zdravkovich. Flow around a circular cylinder near a plane boundary. *Journal of Fluid Mechanics*, 89(1): 33 – 47, 1978.

[23] W. L. Oberkampf and F. G. Blottner. Issues in computational fluid dynamics code verification and validation. *AIAA Journal*, 36(5): 687 – 695, 1998.

[24] M. Casey, and T. Wintergerste. *Best Practice Guidelines*. European Research Community on Flow, Turbulence and Combustion, Version 1.0, 2000.

[25] *TASCflow – Theory Documentation*. Advanced Scientific Computing, Version 2.4, March 1995.

[26] C.M. Rhie. Pressure-based Navier-Stokes solver using the multigrid method. *AIAA Journal*, 27(8): 1017 – 1019.

[27] T.J. Barth, and D.C. Jesperson. The design and application of upwind schemes on unstructured meshes. *AIAA 27th Aerospace Sciences Meeting*, June 27 – 29, 1 – 12, 1989.

[28] R. L. Sani and P. M. Gresho. Resume and remarks on the open boundary condition minisymposium. *International Journal for Numerical Methods in Fluids*, 18: 983 – 1008, 1994.

[29] F. M. White. *Viscous Fluid Flow*. McGraw-Hill, New York, 1974.

[30] Milton Van Dyke. *An Album of Fluid Motion*. The Parabolic Press, Stanford, California, 1982.

[31] L. Zovatto and G. Pedrizzetti. Flow about a circular cylinder between parallel walls. *Journal of Fluid Mechanics*, 440: 1 – 25, 2001.

[32] J.H. Ferziger and M. Peric. *Computational Methods for Fluid Dynamics*. Springer, Berlin, 2002.

Appendix A

Blasius Boundary Layer Simulations

A simple, rectangular prismatic geometry was selected to examine the influence of grid refinement on straightforward Blasius boundary layer simulations. The domain size was selected to be 5mm deep by 50 mm wide by 25 mm high. The Reynolds number with respect to plate length was selected to be 32 360. The grids consisted of an inflation layer adjacent to the solid boundary, which consists of high aspect ratio, stacked, triangular prisms, and tetrahedral elements for the remainder of the domain. A total of 6 grids were considered, with the total number of inflation layers being 5, 10, 20, 30, 40, and 50, corresponding to grids 1 through 6, respectively. The momentum thickness, displacement thickness, and wall friction coefficient were examined. At the midpoint of the domain, the variation of momentum thickness and displacement thickness is shown in Figures A.1 and A.2. The variation of wall friction coefficient with streamwise direction is shown in Figure A.3.

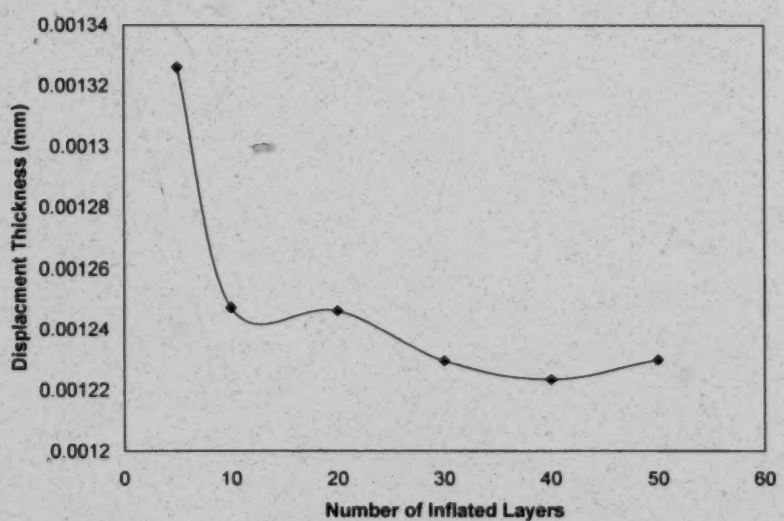

Figure A.1 The variation of displacement thickness with grid refinement.

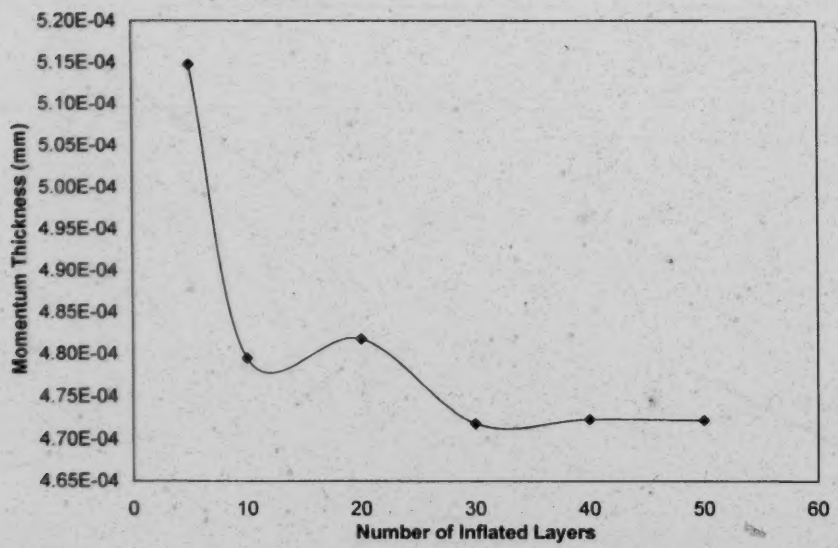

Figure A.2 The variation of momentum thickness with grid refinement.

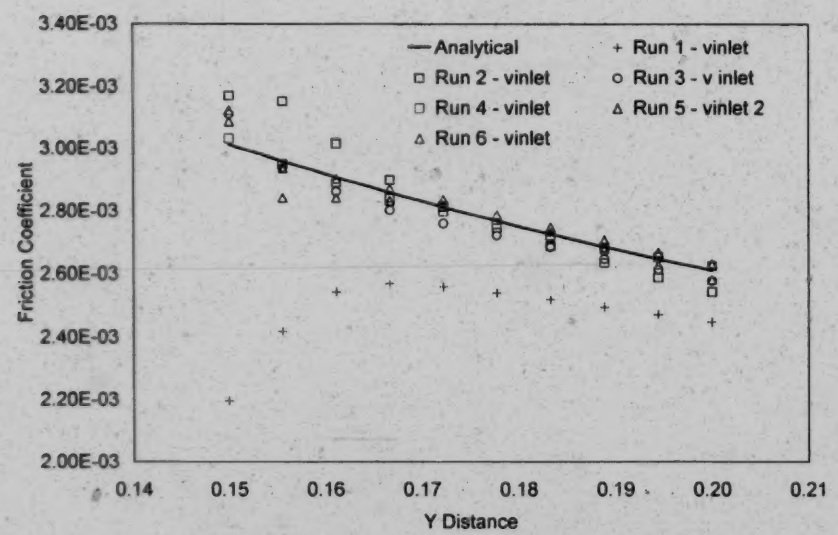

Figure A.3 The variation of friction coefficient in the domain with grid refinement.

Appendix B

Code

The inlet boundary utilised in this research consists of a supplied velocity profile. The velocity profile is a fully-developed Blasius boundary layer. The code presented in this appendix solves the Blasius equation using a shooting method and linearly interpolates the velocity profile to match a given node distribution on an inlet boundary.

```
%This program solves the Blasius flat-plate laminar Eqn (ODE)
%using a shooting method with Runge-Kutta. The boundary layer is outputed
%to a text file.

clear

tspan=[0 10];
maxerr=0.000001;
error=1;
maxit=100;
n=0;
options = odeset('RelTol',1e-9,'AbsTol',[1e-9 1e-9 1e-9]);

yold0=[0 0 1];
[t,yold]=ode45(@rhs,tspan,yold0,options);
ynew0=[0 0 0.5];
[t,ynew]=ode45(@rhs,tspan,ynew0,options);

while (n<maxit) & (error>maxerr)
   error=(abs(ynew(length(ynew),2)-
yold(length(yold),2)))/abs(ynew(length(ynew),2));
   n=n+1;
   m=(ynew(length(ynew),2)-yold(length(yold),2))/(ynew0(3)-yold0(3));

   yold=ynew;
   yold0=ynew0;
   ynew0(3)= (1-yold(length(yold),2) + m*yold0(3))/m;

   [t,ynew]=ode45(@rhs,tspan,ynew0,options);
end

function rhs=rhs(t,y)
rhs=[y(2);y(3); -0.5*y(1)*y(3);];
end
```

```
%----------COMPARISON of ACTUAL to NUMERICAL----------
ada=[0:0.5:8];
fprime=[0 0.1659 0.3298 0.4868 0.6298 0.7513 0.8460 0.9130 ...
  0.9555 0.9795 0.9915 0.9969 0.999 0.9997 0.9999 1 1];
figure(1)        %plot of f'
plot(t,ynew(:,2));
hold
plot(ada,fprime,'ro');
M=[t,ynew(:,2)];
MM=[t.*ynew(:,2)-ynew(:,1)];
dlmwrite('blasius.dat',M,'precision',12);
dlmwrite('vertvel.dat',MM,'precision',12);

% The following program interpolates a Blasius velocity profile onto a supplied file
%of node heights.

uinf=input('enter freestream velocity, m/s: ');
xpos=input('enter the x-position, m: ');
nu=0.01; %1.831e-5/1.185;
M=dlmread('blasius.dat');
I=dlmread('height.txt');
MM=dlmread('vertvel.dat');

scale = sqrt(nu*xpos/uinf);
z=M(:,1)*scale;
uana=M(:,2)*uinf;
ada=I./sqrt(nu*xpos/uinf);
adaAN=M(:,1);

%---------Interpolate to find horizontal velocity ------------------
for i =1:length(I)        %loop for all I values
   a=find(z>I(i));
   a=a(1);
   u(i)=(I(i)-z(a-1))/(z(a)-z(a-1))*(uana(a)-uana(a-1))+uana(a-1);
end

%---------Interpolate to find vertical velocity--------------------
for i = 1:length(I)
   b=find(adaAN>ada(i));
   b=b(1);
   v(i)=(ada(i)-adaAN(b-1))/(adaAN(b)-adaAN(b-1))*(MM(b)-MM(b-1))+MM(b-1);
end
V=uinf.*0.5/sqrt(uinf*xpos/nu).*v;
%-----------------------------------------------------------------

figure(1)
```

```
plot(uana,z);
hold
plot(u,I,'o')
axis([0 1.05*uinf 0 1.05*max(I)]);

figure(2)
plot(V,I,'o')
format long

%----------Write files used for inlet velocity----------
dlmwrite('inletBCu.txt',u','precision',12);
dlmwrite('inletBCv.txt',V','precision',12);
```